Monthly Notices
of the
ROYAL ASTRONOMICAL SOCIETY

MNRAS **504,** 4143–4159 (2021)
Advance Access publication 2021 April 15

doi:10.1093/mnras/stab1048

The cold dust content of the nearby galaxies IC 5325, NGC 7496, NGC 7590, and NGC 7599

Swapnil Singh,[1‹ †] M. L. N. Ashby,[2‹] Sarita Vig,[1‹] S. K. Ghosh,[3] T. Jarrett,[4]
T. M. Crawford,[5,6] Matthew A. Malkan,[7] M. Archipley[8] and J. D. Vieira[8]

[1]*Indian Institute of Space Science & Technology, Thiruvananthapuram 695547, Kerala, India*
[2]*Center for Astrophysics | Harvard & Smithsonian, 60 Garden Street, Cambridge, MA 02138, USA*
[3]*Tata Institute of Fundamental Research, Colaba, Mumbai 400005, India*
[4]*Department of Astronomy, University of Cape Town, Private Bag X3, Rondebosch 7701, South Africa*
[5]*Department of Astronomy and Astrophysics, University of Chicago, 5640 South Ellis Avenue, Chicago, IL 60637, USA*
[6]*Kavli Institute for Cosmological Physics, University of Chicago, 5640 South Ellis Avenue, Chicago, IL 60637, USA*
[7]*Department of Physics and Astronomy, UCLA, Los Angeles, CA 90095-1547, USA*
[8]*Department of Astronomy, University of Illinois at Urbana-Champaign, 1002 West Green Street, Urbana, IL 61801, USA*

Accepted 2021 April 12. Received 2021 April 2; in original form 2021 February 25

ABSTRACT

Star-forming galaxies are rich reservoirs of dust, both warm and cold. But the cold dust emission is faint alongside the relatively bright and ubiquitous warm dust emission. Recently, evidence for a very cold dust (VCD) component has also been revealed via millimetre/submillimetre (mm/sub-mm) photometry of some galaxies. This component, despite being the most massive of the three dust components in star-forming galaxies, is by virtue of its very low temperature, faint and hard to detect together with the relatively bright emission from warmer dust. Here, we analyse the dust content of a carefully selected sample of four galaxies detected by *IRAS*, *WISE*, and South Pole Telescope (SPT), whose spectral energy distributions (SEDs) were modelled to constrain their potential cold dust content. Low-frequency radio observations using the Giant Metrewave Radio Telescope (GMRT) were carried out to segregate cold dust emission from non-thermal emission in mm/sub-mm wavebands. We also carried out *AstroSat*/Ultraviolet Imaging Telescope (UVIT) observations for some galaxies to constrain their SED at shorter wavelengths so as to enforce energy balance for the SED modelling. We constructed their SEDs across a vast wavelength range (extending from UV to radio frequencies) by assembling global photometry from *GALEX* FUV + NUV, UVIT, Johnson BRI, 2MASS, *WISE*, *IRAC*, *IRAS*, *AKARI*, *ISOPHOT*, *Planck* HFI, SPT, and GMRT. The SEDs were modelled with CIGALE to estimate their basic properties, in particular to constrain the masses of their total and VCD components. Although the galaxies' dust masses are dominated by warmer dust, there are hints of VCD in two of the targets, NGC 7496 and NGC 7590.

Key words: dust, extinction – galaxies: fundamental parameters – infrared: galaxies – radio continuum: galaxies – submillimetre: galaxies.

1 INTRODUCTION

Dust grains play an important role in the heating and cooling of the interstellar medium (ISM; Wolfire et al. 1995). They are responsible for absorbing nearly half of the total stellar radiation over the lifetime of the Universe (Lagache, Puget & Dole 2005). This absorbed energy is then re-emitted as thermal radiation at far-infrared (FIR) and submillimetre (sub-mm) wavelengths (Wolfire et al. 1995). Dust enmeshed in cold, dense molecular clouds plays a significant role in star formation, and is in some ways a better probe of the cold ISM than the low-lying lines of ^{12}CO or molecular lines seen at high optical depths (Israel 1997; Scoville et al. 2014). Detailed observations of dust in the Milky Way (MW) and other galaxies have thus far revealed only an incomplete picture of the physical and chemical properties of dust. Thus, our lack of knowledge of the humble dust grains limits our understanding of their role in star formation and galaxy evolution (Li & Greenberg 2003).

FIR/sub-mm emission from dust strongly depends on the properties of the grains and the environment where they reside (Witt & Gordon 2000; Misselt et al. 2001). The FIR output tends to peak at $\sim 100\,\mu$m. At sub-mm wavelengths, the Rayleigh–Jeans tail of dust emission becomes optically thin even at high column densities [e.g. $N(\mathrm{H_2}) \sim 2\times 10^{24}\,\mathrm{cm^{-2}}$ at 300 μm; Scoville et al. 2014; Pagani et al. 2015]. Thus, the total dust content in a galaxy can be estimated for a given dust emissivity per unit mass (Draine et al. 2007). In reality, FIR/sub-mm emission from a star-forming galaxy is produced by multiple components over a continuous range of temperatures. None the less, many studies, such as Cox, Kruegel & Mezger (1986) and Galametz et al. (2011), model the FIR emission beyond 40–50 μm

---

E-mail: swapnils@ursc.gov.in (SS); mashby@cfa.harvard.edu (MLNA); sarita@iist.ac.in (SV)

† Present address: Space Astronomy Group, U. R. Rao Satellite Centre, Bangalore 560037, India.

© 2021 The Author(s)
Published by Oxford University Press on behalf of Royal Astronomical Society

Downloaded from https://academic.oup.com/mnras/article/504/3/4143/6226636 by University of Chicago user on 31 May 2021

with three discrete dust components: (i) very cold dust (VCD, 11–14 K) associated with quiescent molecular clouds, (ii) cold dust (15–25 K) associated with atomic hydrogen, and (iii) warm dust (30–40 K) associated with ionized gas in low-density H II regions and warm molecular gas. There is an additional hot dust component having temperatures up to ~ 2000 K, which is seen in active galactic nuclei (AGNs; Lira et al. 2013; Netzer 2015). This component, coming from the AGN accretion and powerful shocks, is seen in the near-infrared (NIR) and mid-infrared (MIR) regimes.

Models such as these, although they are simplifications, are highly successful and are widely used to characterize the physical properties of the galaxies' dust and ISM (Casey, Narayanan & Cooray 2014; Ciesla et al. 2014; Scoville et al. 2014). The terminology used for dust components varies from author to author (Galametz et al. 2011; Dale et al. 2012; Kirkpatrick et al. 2013; Lanz et al. 2013). Throughout this paper, we follow the previously mentioned convention of very cold, cold, and warm dust components.

Local star-forming galaxies serve as a laboratory to study star formation properties of galaxies that drive the evolution of the galaxy. Star-forming galaxies generate large ultraviolet (UV) fluxes, due to the presence of young O- and B-type stars, which are absorbed and then re-radiated in the infrared (IR) by the dust. Up to 90 per cent of a galaxy's UV emission can be shifted into the FIR regime in this way (Buat et al. 2010). Thus, the total dust mass in a star-forming galaxy can be used as a tracer of the young stellar population as well as the star-forming potential of the galaxy (Gould & Salpeter 1963; van Dishoeck 2004). Warm dust primarily traces the recently formed young massive stars while cold dust traces the dense molecular clouds from which stars form. VCD emission peaks in the millimetre/submillimetre (mm/sub-mm) regime and the coldest dust component dominates the dust mass despite its small contribution to the total FIR emission (Clemens et al. 2013).

For example, Stark et al. (1989) showed that the emission at wavelengths longer than 12 μm contributes to about one-third of the total flux in some spiral galaxies in the Virgo cluster. Several other, more recent studies have also examined the relation between cold dust and star formation. Galametz et al. (2010) found that the cold and warm dust emission in NGC 6822 are correlated and hence the cold dust emission also traces star formation, in addition to the warm dust. Clemens et al. (2013) argue that the temperature of the cold dust component is weakly correlated with the ratio of star formation rate (SFR) and the dust mass. As a consequence, modelling the dust emission for a galaxy can be used to decipher the SFR in the galaxy.

Various FIR/sub-mm observatories such as the *Spitzer Space Telescope* (Werner et al. 2004), *AKARI* (Murakami et al. 2007), *Herschel* (Pilbratt et al. 2010), *Planck* (Planck Collaboration & Lawrence 2011), and the South Pole Telescope (SPT; Carlstrom et al. 2011) have made it possible to investigate the properties of cold dust in nearby galaxies (Hippelein et al. 2000; Thuma et al. 2000; Marleau et al. 2004; Matthews et al. 2008; Rowan-Robinson et al. 2010; Tabatabaei et al. 2013). There are tantalizing hints in the *Herschel* imaging for the presence of a VCD component in nearby galaxies, such as NGC 1140, NGC 4826, NGC 7674, NGC 7793, and the KINGFISH sample (Galametz et al. 2011, 2014; Dale et al. 2012). But the evidence for the presence of this component so far remains ambiguous (Bot et al. 2010; Rowlands et al. 2014). Pagani et al. (2015) used FIR/sub-mm emission across L183, a cold dark cloud, to demonstrate that VCD exists but is difficult to identify solely by its emission. This may lead to an underestimation of the dust mass. Some authors also report an anomalous dust emission in the microwave regime (~ 10–90 GHz) produced possibly due to rapidly rotating very small dust grains having a non-zero electric dipole moment (Draine & Lazarian 1998; Murphy et al. 2010). Another major challenge is the removal of the potential contamination by thermal and non-thermal radio emission from the VCD in the mm/sub-mm regimes (Condon 1992; Bot et al. 2010).

In star-forming galaxies, thermal free–free radiation originates in H II regions and is optically thin. Non-thermal synchrotron radiation, on the other hand, is emitted by relativistic electrons accelerated in the galactic magnetic fields and is usually modelled as a power law. Although modelling the non-thermal emission is a complex process, simple approximations can be used to estimate the SFRs (Condon 1992). While the obtained SFRs are consistent with the available values from other SFR indicators, better estimates of supernova rates are needed to strengthen the relationship between the non-thermal emission and SFR. As this non-thermal emission contributes at mm wavelengths, a reliable spectral energy distribution (SED) modelling scheme is essential to obtain precise measurements of masses of the total and VCD components in a star-forming galaxy.

Towards this objective, we selected four low-redshift southern star-forming galaxies based on the criteria discussed in Section 2. Our observations are presented in Section 3 and the results are discussed in Section 4. The construction of SEDs and their modelling is presented in Section 5. The nature of evidence of a VCD component in these galaxies is discussed in Section 6. Finally, the results are summarized in Section 7.

2 THE PILOT SAMPLE

The estimation of accurate dust masses entails sub-mm and mm observations because the warm dust emission dominates at shorter wavelengths (Galametz et al. 2011; Bendo et al. 2012). For this work, we therefore selected low-redshift galaxies that were observed by the SPT in three broad-bands at frequencies corresponding to 1.4, 2.0, and 3.2 mm. In order to obtain significant detections, we chose galaxies with flux densities > 10 mJy in the 1.4 mm SPT band. We restricted the sample to galaxies having spectral indices α below 1.66, where α is defined through the relation $S_\nu \propto \nu^\alpha$ and measured between the SPT 1.4 and 3.2 mm bands to ensure that synchrotron emission does not dominate their sub-mm emission. We also imposed a requirement that the targets be detected by both *IRAS* and *WISE* so that the warm dust component can be modelled reliably. A size constraint was applied such that the galaxy size along the major axis < 5 arcmin in the *WISE* 22 μm maps, for the reliable recovery of their fluxes in the SPT bands. These galaxies were detected by the Sydney University Molonglo Sky Survey (SUMSS; Mauch et al. 2003) at 843 MHz that provides useful constraints on their non-thermal radio emission.

A pilot sample of four galaxies visible from the Giant Metrewave Radio Telescope (GMRT), which satisfied all these conditions, was constructed: IC 5325, NGC 7496, NGC 7590, and NGC 7599. Each galaxy is a spiral with low or moderate SFRs ranging between 0.3 and 6 M yr^{-1}, based on SFR estimators spanning the electromagnetic spectrum, including both continuum and line emission (Kennicutt 1983; Schmitt et al. 2006; Muñoz-Mateos et al. 2007; Thilker et al. 2007). Some of the indicators include UV, H α, IR, and radio luminosities (Kennicutt 1998a). All four galaxies belong to the same southern group of galaxies (Garcia 1993). Two of the galaxies in the sample, NGC 7590 and NGC 7599, also belong to the Grus-Quartet (a group of four interacting galaxies) along with two other members of the larger group, NGC 7552 and NGC 7582 (Koribalski 1996; Freeland, Stilp & Wilcots 2009). Basic data for our sample of four galaxies are listed in Table 1.

Downloaded from https://academic.oup.com/mnras/article/504/3/4143/6226636 by University of Chicago user on 31 May 2021

Table 1. Basic parameters for the sample of galaxies used in this work, taken from NASA/IPAC Extragalactic Database (NED).

Galaxy	RA, Dec. (J2000) (hh:mm:ss, dd:mm:ss)	z	Distance (Mpc)	Diameter (arcmin)	Morphology	Activity type	SFR (M yr^{-1})	log $M_{\star}$ ^{a} (M)
IC 5325	23:28:43.43, −41:20:00.5	0.00501	17	2.8	SAB(rs)bc	–	0.31^{b}, 0.41^{c}	10.12
NGC 7496	23:09:47.29, −43:25:40.6	0.00550	19	3.3	SB(s)b	Seyfert 2	0.81^{d}, 1.35^{d}, 2.20^{d}, 1.73^{d}, 1.97^{d}, 0.31^{c}	9.94
NGC 7590	23:18:54.81, −42:14:20.6	0.00526	18	3.4	SA(rs)bc	Seyfert 2	6.20^{e}	10.08
NGC 7599	23:19:21.14, −42:15:24.6	0.00551	19	4.4	SA(s)c	–		10.03

[a] Jarrett et al. (2019).
[b] Thilker et al. (2007).
[c] Muñoz-Mateos et al. (2007).
[d] From different methods described in Schmitt et al. (2006).
[e] Kennicutt (1983).

3 OBSERVATIONS AND DATA REDUCTION

To obtain precise measurements of the cold dust content in galaxies, reliable SED modelling needs to be performed. Multiwavelength observations across the electromagnetic spectrum allow us to model each component in a galaxy, while enforcing energy balance. Towards this objective, we performed radio and UV observations. The radio observations were performed using the GMRT, allowing us to isolate synchrotron emission from the long-wavelength thermal tail of the dust emission at sub-mm/mm wavelengths that was obtained from SPT observations (see Sections 3.1 and 3.2). We also obtained UV imaging using the Ultraviolet Imaging Telescope (UVIT) in order to constrain UV emission from the galaxies (see Section 3.3). This ensures reliable energy balance and derivation of the galaxies' basic properties.

3.1 GMRT radio continuum observations

The synchrotron flux density can contribute significantly to galaxies' mm luminosity. As synchrotron emission is best studied at low frequencies, GMRT is an ideal choice. GMRT (Swarup et al. 1991) consists of 30 parabolic dishes of 45 m diameter each. Of the 30 antennas, 12 are located in a central array within an area of ~ 1 km^2 and 18 are stretched out along three arms in a Y shaped configuration. The shortest and longest baselines are ~ 100 and 25 km, respectively. The number and configuration of the dishes provide a double advantage: high angular resolution as well as the ability to image the extended diffuse radio emission. All four galaxies in the sample were observed using GMRT in 2017 December to 2018 January. The galaxies were observed at 325, 610, and 1300 MHz with a bandwidth of 32 MHz. 3C 48, 3C 138, and 3C 147 were used as flux calibrators and the selected phase calibrators were 0010 − 418 and 2314− 449. In addition, we used archival data for NGC 7590 and NGC 7599 at 610 MHz with 16 MHz bandwidth, taken from the GMRT Online Archive. The details of the observations are presented in Table 2.

The data reduction was carried out using the NRAO's Astronomical Image Processing System. The data sets were carefully checked for corrupted data (due to bad baselines, radio-frequency interference, non-working antennas, etc.) using the tasks `TVFLG`, `UVFLG`, `UVPLT`, and `VPLOT`, which were then removed before proceeding further with the analysis. Calibration was carried out using the tasks `CALIB` and `CLCAL`. To increase the signal-to-noise ratio (SNR), the calibrated data were averaged over several channels. These averaged data were checked again for corrupted data and re-calibrated. These calibrated data were cleaned and deconvolved using the task `IMAGR`, which generates a map of the field using the `CLEAN` algorithm. Multiple iterations of the self-calibration process and `IMAGR` were applied to minimize the amplitude and phase errors. To correct for the loss of sensitivity away from the phase centre, `PBCOR` was used for applying a primary beam correction to each image. After this step, final images were generated using `FLATN`. The root-mean-square (rms) noise and synthesized beam of the final images are listed in Table 2.

3.2 SPT millimetre continuum observations

The SPT (Carlstrom et al. 2011) is a 10 m telescope located at the National Science Foundation Amundsen-Scott South Pole station in Antarctica. Initially the SPT was configured with a single mm-wave camera, the SPT-SZ receiver, equipped with 960 detectors capable of observing in three bands centred at roughly 1.4, 2.0, and 3.2 mm with an angular resolution of 1.0, 1.2, and 1.7 arcmin, respectively. From 2008 to 2011, the SPT carried out the SPT-SZ survey, covering ~ 2500 deg^2 of southern sky in the three sub-mm bands. The SPT-SZ survey covers a contiguous region from 20$^{\mathrm{h}}$ to 7$^{\mathrm{h}}$ in right ascension (RA) and −65° to −40° in declination, and was mapped to depths such that the 1σ point source sensitivity was approximately 4.0, 1.2, and 2.0 mJy at 1.4, 2.0, and 3.2 mm, respectively (Everett et al. 2020). Fig. 1 in Story et al. (2013) shows the field locations and extent of the survey.

Because cold dust emission peaks in the sub-mm/mm regime (Section 1), SPT-SZ photometry formed a key part of the selection criteria (see Section 2), allowing us to select galaxies with significant mm/sub-mm emission. However, our analysis requires a custom treatment of the SPT-SZ data. All previously published SPT data were for sources that were assumed to be unresolved (point-like) at the arcminute angular resolution of the SPT (e.g. Vieira et al. 2010; Mocanu et al. 2013; Everett et al. 2020, and the standard SPT data pipeline treated them appropriately. By contrast, the sources considered in this work are resolved by SPT, so a different approach was needed. Specifically, the time-ordered SPT datastream has to be re-analysed employing methods that accurately accounted for emission falling outside a single SPT beam.

The approach adopted here was to use carefully reprocessed *WISE* 22 µm (Band 4) imaging (Jarrett et al. 2019) as a template for the surface brightness distribution in the SPT bands. We expect the reprocessed *WISE* Band 4 images, with their sensitivity to warm dust, to be a reasonable proxy for the spatial distribution of the colder dust responsible for the bulk of the emission at mm wavelengths, with a relatively small contamination from starlight continuum and

Downloaded from https://academic.oup.com/mnras/article/504/3/4143/6226636 by University of Chicago user on 31 May 2021

Table 2. Summary of GMRT observations.

Galaxy	Frequency (MHz)	Date of observation	On-source time (min)	Synthesized beam	PA (deg)	RMS (mJy per beam)	Peak flux (mJy per beam)	Integrated flux (mJy)
IC 5325	325	8 Jan 2018	182	19.60 arcsec × 9.01 arcsec	−16.43	0.43	2.88	91.0 ± 9.4
	610	7 Jan 2018	181	11.19 arcsec × 4.61 arcsec	20.00	0.04	1.36	66.0 ± 5.1
NGC 7496	325	31 Dec 2017	140	21.44 arcsec × 10.28 arcsec	5.91	0.20	18.99	58.7 ± 5.0
	1300	30 Dec 2017	133	5.33 arcsec × 2.20 arcsec	13.05	0.03	13.05	21.4 ± 3.1
NGC 7590	325	5 Jan 2018	153	22.52 arcsec × 11.05 arcsec	−3.37	0.80	13.77	148.2 ± 14.2
	610	10 Jan 2010	183	10.86 arcsec × 4.94 arcsec	12.54	0.08	12.11	112.0 ± 6.1
NGC 7599	325	5 Jan 2018	153	22.52 arcsec × 11.05 arcsec	−3.37	0.80	8.31	125.8 ± 11.0
	610	10 Jan 2010	183	10.86 arcsec × 4.94 arcsec	12.54	0.08	8.25	84.5 ± 5.3

Note. Errors in the flux densities are estimated using the expression given by Sánchez-Monge et al. (2013), where the uncertainty in the flux calibration of GMRT is taken to be 5 per cent (Lal & Rao 2007).

emission lines (e.g. Izotov et al. 2014). Also, *WISE* has an angular resolution of 12 arcsec in Band 4, much less than those of the SPT beams. Our templates are constructed by fitting two-dimensional Sérsic profiles to the *WISE* 22 μm (Band 4) images (Jarrett et al. 2019).

To extract the SPT flux densities from the maps, a 30 arcmin × 30 arcmin cut-out is first extracted from the SPT-SZ maps, centred on the best-fitting position of the source in the *WISE* imaging. A three- or five-parameter fit is performed on the three cut-outs simultaneously, in which the model is the best-fitting *WISE* Band 4 Sérsic model, convolved with the known filtering kernel and beam for each SPT band. The parameters of the fit are three amplitudes (one for each SPT band) and, in the five-parameter case, offsets in RA and Dec. from the best-fitting *WISE* position to account for any residual astrometry errors in the SPT data. We find no evidence for any such residual error. The fits are performed in Fourier space, and each Fourier mode is weighted by its expected inverse noise squared. The noise model is the sum of instrument noise (assumed to be white, or uncorrelated between map pixels and bands) and anisotropy in the cosmic microwave background (CMB). The pixel–pixel and band–band correlation in the CMB contribution is properly taken into account. No explicit contribution from the atmosphere is included in the noise model, because the behaviour of atmospheric contamination is significantly similar to that of the CMB in these fits, particularly in the very red angular spectrum. We derive the final parameter covariance from simulated observations. For each of the sources in this work, we inject a signal into the true SPT maps near the location of the true source, extract the map cut-out at the simulated source location, and estimate the flux density of the simulated source in the same manner as with the true sources. The injected signal near each true source is the *WISE* Band 4 model, convolved with the SPT filtering kernel and beam, and scaled so that the expected SNR on the amplitude is roughly 10 in each band. We repeat the procedure 400 times for each source.

We calculate a three-element residual vector for each source and realization, equal to the extracted best-fitting flux density minus the known input flux density in each band, and we use the mean of the outer product of that residual vector over the 400 realizations as our covariance matrix. As expected, the simulation-based uncertainties differ from those calculated using the noise model (by ~60 per cent at 1.4 mm, and ~20 per cent at 3.2 mm). The off-diagonal components of the final covariance matrix are < 10 per cent, so we report the flux densities in the three SPT bands in Table A1 with uncorrelated uncertainties.

3.3 AstroSat – UVIT ultraviolet observations

Two galaxies in the sample, NGC 7590 and NGC 7599, were imaged using the UVIT on-board the *AstroSat*. *AstroSat* is the first Indian Space Observatory (Agrawal 2004; Singh et al. 2014) that observes simultaneously in X-rays (0.3–100 keV), UV and visible wavelengths. UVIT is an imaging instrument comprised of two co-aligned telescopes in a Ritchey–Chretien configuration, each having an aperture of 375 mm. The instrument covers a circular field of view of ~28 arcmin diameter. One of the telescopes observes in FUV (1300–1800 Å), the other in NUV (2000–3000 Å), and visible (3200–5500 Å). Each channel (FUV, NUV, and visible) has several selectable filters with narrower passbands. The spatial resolution achieved by UVIT in FUV/NUV and the visible channel is < 1.5 and < 2.2 arcsec, respectively. More details about the instrument and its in-orbit calibrations and performance can be obtained from Tandon et al. (2017a,b).

NGC 7590 and NGC 7599 were observed by UVIT on 2017 November 30, in two FUV filters (*F154W* and *F172M*) and two NUV filters (*N245M* and *N279N*). The details of the observations and filters are listed in Table 3. Simultaneous imaging in a neutral density visible filter was used for aspect reconstruction during the post-observation data processing stage. The Level-1 data products made available by the Indian Space Science Data Center (ISSDC/ISRO) were processed using the UVIT Level-2 Pipeline (UL2P) version V6.3. The pipeline corrects for various instrumental effects (spacecraft drifts, jitter, thermal effects, etc.). The UL2P gave the images of the sky in the field of view as the final products, with a pixel size of 0.42 arcsec × 0.42 arcsec. The intensity unit of the images is counts/sec (CPS). The integrated CPS for all the galaxies for each filter were converted to flux densities ($F_{\rm filter}$) and AB magnitudes ($m_{\rm AB}$) using the following relations as per the prescription of Tandon et al. (2017a):

$$\begin{aligned} F_{\rm filter} &= {\rm CPS} \times {\rm UC}\ ({\rm erg\ s^{-1}\ cm^{-2}}\ \mathring{\rm A}^{-1}), \\ m_{\rm AB} &= -2.5\log({\rm CPS}) + {\rm ZP}. \end{aligned} \tag{1}$$

The values of zero-point (ZP) magnitudes and unit conversion (UC) factors are listed in Table 3. The uncertainties in flux densities for each filter are taken as 5 per cent considering (i) the uncertainties in CPS arising from Poisson noise of the photon-counting detector and (ii) the error in the UC factor from calibration uncertainties (Subramaniam et al. 2016).

The obtained flux densities have been corrected for foreground extinction in the MW. Adopting the ratio of total-to-selective extinction as $R_V = 3.1$ (Whitford 1958) for the MW, the extinction coefficient in *V* band (A_V) was calculated for each of the galaxies. Using the

Downloaded from https://academic.oup.com/mnras/article/504/3/4143/6226636 by University of Chicago user on 31 May 2021

Table 3. Details of *AstroSat* – UVIT observations.

Band	Filter	λ_{mean} (Å)	λ (Å)	Zero-point magnitude	Unit conversion ($\times 10^{-15}$)	Exposure time (s)
FUV	*F*154*W*	1541	380	17.765 ± 0.010	3.593 ± 0.040	3221
FUV	*F*172*M*	1717	125	16.341 ± 0.020	10.710 ± 0.160	2593
NUV	*N*245*M*	2447	280	18.500 ± 0.070	0.725 ± 0.004	2723
NUV	*N*279*N*	2792	90	16.500 ± 0.010	3.500 ± 0.035	6420

Table 4. Details of extinction and UVIT flux densities for galaxies in our sample.

Galaxy	Band	Extinction (A_λ)	Flux density (mJy)
NGC 7590	*F*154*W*	0.123	8.49 ± 0.42
	*F*172*M*	0.118	9.87 ± 0.49
	*N*245*M*	0.114	10.99 ± 0.55
	*N*279*N*	0.092	13.44 ± 0.67
NGC 7599	*F*154*W*	0.126	8.92 ± 0.45
	*F*172*M*	0.120	10.78 ± 0.54
	*N*245*M*	0.116	12.70 ± 0.64
	*N*279*N*	0.094	17.53 ± 0.88

reddening relation of Cardelli, Clayton & Mathis (1989), this A_λ was used to estimate and correct for the extinction in each filter, as listed in Table 4.

4 RESULTS

4.1 Radio emission from the galaxies

The distribution of radio emission from ionized gas in galaxies can help us understand the emission mechanism and provide hints about the star formation activity in addition to possible activity from a central black hole. The GMRT has a minimum baseline of ~100 m and is thus able to detect large structures up to a size of 32, 17, and 9 arcmin at frequencies of 325, 610, and 1300 MHz, respectively. Each galaxy in our sample has a diameter <5 arcmin. Thus, the GMRT is capable of detecting most of the galaxies' emission at these frequencies and it is unlikely that any diffuse emission has been missed. The radio emission from our sample of galaxies is shown as contours in Fig. 1. The details of the emission from each galaxy are discussed below:

IC 5325: The 325 and 610 MHz maps suggest that the emission is spread over the disc with the peak emission being close to the centre of the galaxy.

NGC 7496: The emission at 325 MHz is distributed across the galaxy with the peak emission at the centre of the galaxy. We note that the emission traces one of the spiral arms in the galaxy. The 1300 MHz emission is detected solely towards the nucleus of the galaxy, which might be due to the presence of an AGN.

NGC 7590: The emission at both frequencies (325 and 610 MHz) is distributed throughout the galaxy.

NGC 7599: We observe that the emission at both 325 and 610 MHz peaks in one of the spiral arms of the galaxy. This region outshines the rest of the galaxy as not much emission is seen from the other regions in the galaxy. This may indicate some intense star formation activity happening in that spiral arm of the galaxy. Alternately, it is possible that this is an effect of superposition of emission from an alternate radio source in the sky. But this hotspot also lies towards the H I 'bridge' linking NGC 7599 and NGC 7590 as seen by Freeland et al. (2009). This implies that the two galaxies are interacting and argues against the chance-superposition hypothesis. We also see a high UV flux in the region, which is indicative of young star formation (see Section 4.2).

We combined the GMRT detections with all other available radio flux measurements to construct the radio SEDs of these galaxies. The VLA flux densities were obtained from NED, while the 843 MHz flux densities from SUMSS (Sadler & Hunstead 2001) were extracted from the images obtained from their archive.[1] We estimated the spectral indices α adopting the standard definition (see Section 2). The value of $\alpha = -0.1$ indicates thermal optically thin emission, while for synchrotron optically thin emission typically $\alpha = -0.8$. The spectral indices for the galaxies were calculated using two methods: (i) using GMRT flux densities alone and (ii) using all available flux measurements from multiple interferometric observations. The former was carried out by restricting the GMRT image visibilities to the same *UV* range ($\sim 95\lambda$ to $23\mathrm{k}\lambda$) so that fluxes within the same spatial scales are considered. In the latter method, the flux densities from all available images were used although they were taken with different array configurations. As a consequence, the spectral indices from the latter method can be considered approximate at best. The spectral indices are listed in Table 5 and shown as lines in Fig. 2.

4.2 UV emission from galaxies

The UV images of NGC 7590 and NGC 7599 from UVIT are shown in Fig. 1. For the other two galaxies, we have considered the images taken by the *Galaxy Evolution Explorer* (*GALEX*). In each of the image panels, we have also included the DSS optical images in the top right. The UV images trace the location of young stars in the galaxies, with dominant contribution from OB stars. The optical images, on the other hand, trace the older stellar population. Kennicutt & Evans (2012) suggest that the NUV and FUV emission trace recent star formation with stars having ages up to 200 and 100 Myr, respectively. We briefly describe the morphology of these galaxies in the UV regime and compare them with optical.

In IC 5325, the *GALEX* UV emission appears to trace the fragmented arms of the galaxy. The emission is mostly from the inner regions of the disc. The galaxy is brighter in FUV as compared to NUV, which implies that recent star formation has occurred in the galaxy in the last 100 Myr. The optical image for IC 5325 shows that the inner disc of the galaxy is dominated by late-type stars. In NGC 7496, we see strong emission in both NUV and FUV from the centre of the galaxy as well as clumpy emission from the two spiral arms. The northern spiral arm shows traces of young massive stellar complexes unlike the southern arm, where regions towards the ends of the arms indicate the presence of young stellar complexes. This suggests that these regions are composed of young stars having ages

---

[1] http://www.astrop.physics.usyd.edu.au/cgi-bin/postage.pl

Downloaded from https://academic.oup.com/mnras/article/504/3/4143/6226636 by University of Chicago user on 31 May 2021

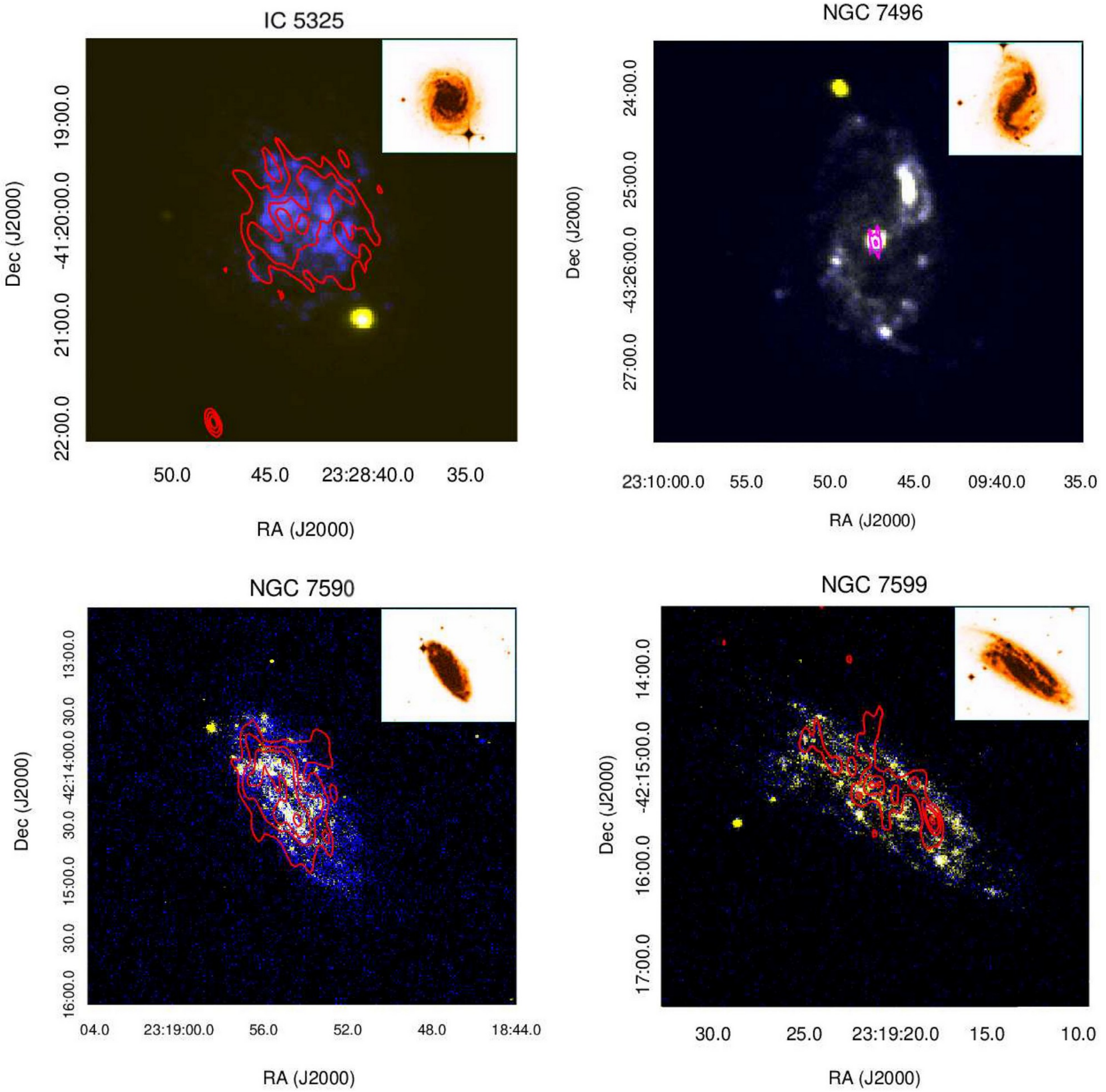

Figure 1. Colour composite UV images (NUV: yellow and FUV: blue) for the galaxies in the sample overlaid with GMRT 1300 MHz (magenta) and 610 MHz (red) contours. The DSS images for each galaxy (3.8 arcmin × 3.2 arcmin) are shown in the top right corner of each panel. Top left: *GALEX* image for IC 5325 overlaid with 610 MHz contours. The contour levels are 15, 20, 25, and 30 times σ where $\sigma = 38\,\mu$Jy per beam. Top right: *GALEX* image for NGC 7496 overlaid with 1300 MHz contours. The contour levels are 20, 35, and 215 times σ where $\sigma = 28\,\mu$Jy per beam. Bottom left: UVIT image for NGC 7590 overlaid with 610 MHz contours. The contour levels are 15, 25, 40, and 45 times σ where $\sigma = 78\,\mu$Jy per beam. Bottom right: UVIT image for NGC 7599 overlaid with 610 MHz contours. The contour levels are 15, 25, 40, and 45 times σ where $\sigma = 78\,\mu$Jy per beam.

Table 5. Radio spectral indices for the galaxies in our sample.

Galaxy	IC 5325	NGC 7496	NGC 7590	NGC 7599
Spectral index from GMRT	−0·51 ± 0·72[a]	−0·42 ± 0·14[b]	−0·46 ± 0·25[a]	−0·63 ± 0·24[a]
Spectral index from all radio data	−1.04 ± 0.32	−0.61 ± 0.12	−0.64 ± 0.06	−0.62 ± 0.24

[a] 325−610 MHz.
[b] 325–1300 MHz.

between 0 to 200 Myr. In this galaxy, the emission from the older stellar population comes from the centre of the galaxy as well as the two arms. In NGC 7590, UV emission traces the spiral arms of the galaxy with more younger stars located in the inner regions of arms close to the centre of the galaxy. In this galaxy as well, an equal emission from NUV and FUV is observed indicating stellar ages in the range 0–200 Myr. From the optical image of NGC 7590, we see that the old stellar population is well distributed throughout

Downloaded from https://academic.oup.com/mnras/article/504/3/4143/6226636 by University of Chicago user on 31 May 2021

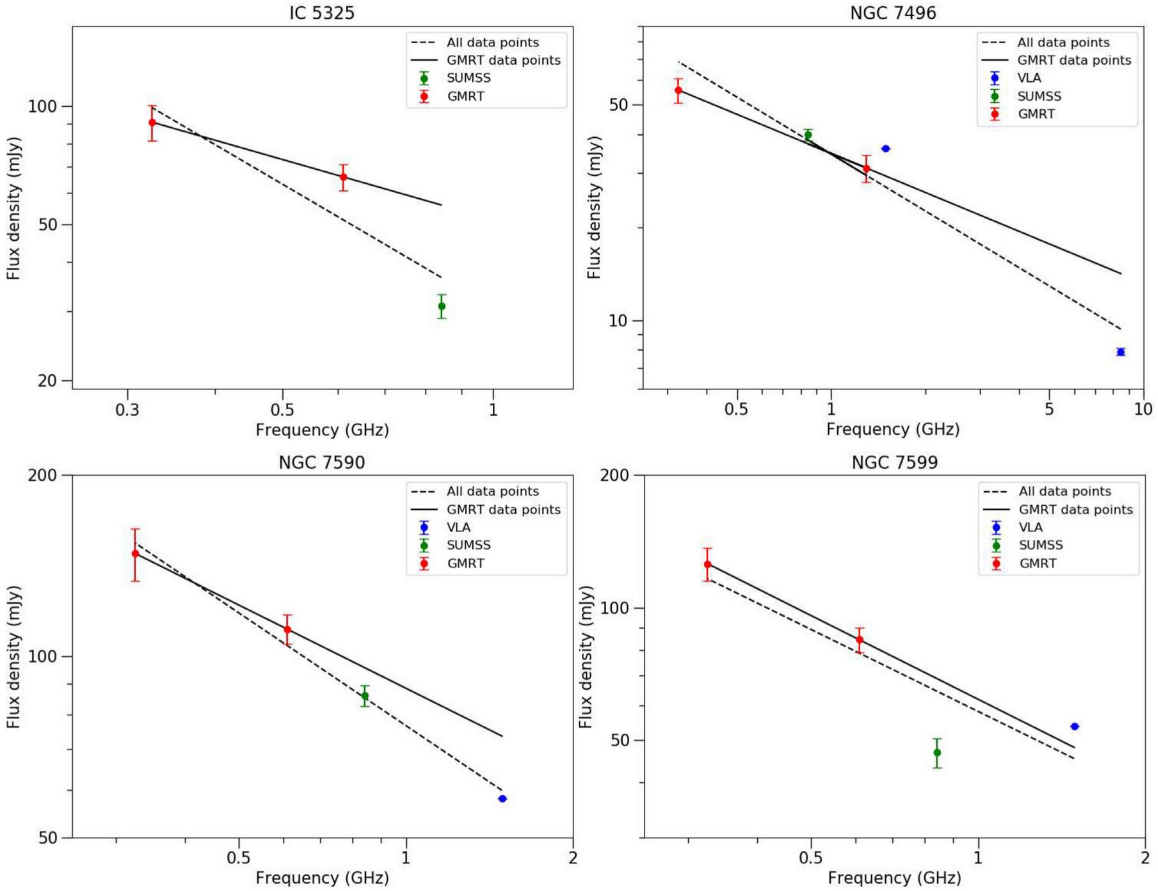

Figure 2. Radio-frequency SEDs for the pilot sample. The red, green, and blue data points are flux densities from GMRT, SUMSS, and VLA, respectively. The solid line indicates the spectral slope calculated from the GMRT data only while the dashed line indicates the spectral slope inferred from all available data.

the disc of the galaxy. For NGC 7599, the images generated from UVIT observations show that the UV emission traces the spiral arms of the galaxy. A similar trend is seen in the optical image as well. The composite UV image shows that the galaxy is dominated mostly by NUV emission with young stars having an age of up to 200 Myr. From the FUV image of this galaxy, we observe that the same region having high flux in the radio image has marginally higher emission than that from the surrounding regions in the galaxy. The optical image also shows that this region does not have a significant older population as compared to the young stellar population.

4.3 Integrated star formation rates of the galaxies

The SFR of a galaxy constrains its evolutionary history. Most of the methods for SFR estimation are derived from correlations in large galaxy samples. These correlations are not very tight and could introduce an inherent selection bias in the SFR relations. The derived SFRs are usually highly uncertain in galaxies due to lack of information regarding (i) details of various physical processes contributing to star formation in the galaxy and (ii) precise estimates of physical conditions in the galaxy. Nevertheless, the SFR of a galaxy provides useful insights regarding its evolution and can be used for comparison of SFRs with other galaxies, derived using similar methods.

The SFRs of the sample of galaxies from literature are listed in Table 1 and their values differ depending on the wavelength used. In the current work, we compare the SFRs obtained by employing IR (60 µm), FIR and radio (610 MHz) flux densities as well as FUV (UVIT/*GALEX*) absolute magnitudes.

The SFR estimated using the 60 µm flux density (ψ) is given by the following relation from Rowan-Robinson et al. (2008).

$$\frac{\psi}{\mathrm{M}\ \ \mathrm{yr}^{-1}} = 2.2\ ^{-1}10^{-10}\ \frac{L_{60}}{\mathrm{L}}\ . \tag{2}$$

Here, = 2/3 represents the fraction of UV light absorbed by dust.

We also estimated the galaxies' SFRs using the FIR luminosity following the method prescribed by Kewley et al. (2002):

$$\mathrm{SFR_{IR}}\ (\mathrm{M}\ \ \mathrm{yr}^{-1}) \sim 7.9 \times 10^{-44} L_{\mathrm{FIR}}\ (\mathrm{erg\ s}^{-1}), \tag{3}$$

where L_{FIR} is the FIR luminosity computed from the *IRAS* 60 and 100 µm fluxes, and the distance to the galaxy.

At 610 MHz, Garn et al. (2009) provide two ways to estimate the galaxy SFR (φ) depending on galaxy luminosity. This treatment includes the effect of non-thermal emission assuming a spectral index of −0.8.

$$\frac{\varphi}{\mathrm{M}\ \ \mathrm{yr}^{-1}} = 2.84 \times 10^{-22}\ \frac{L_{610}}{\mathrm{W\ Hz}^{-1}}\ \ ;\ L_{610} > L_{\mathrm{c}}, \tag{4}$$

$$\frac{\varphi}{\mathrm{M}\ \ \mathrm{yr}^{-1}} = \frac{2.84 \times 10^{-22}}{0.1 + 0.9(L_{610}/L_{c})^{0.3}}\ \frac{L_{610}}{\mathrm{W\ Hz}^{-1}}\ \ ;\ L_{610} \leq L_{\mathrm{c}}. \tag{5}$$

Here, $L_{\mathrm{c}} = 3.3 \times 10^{21}$ W Hz^{-1} is the luminosity at 610 MHz of an $\sim L_{*}$ galaxy with $\varphi \sim 1$ M yr^{-1}.

We also estimated the SFRs using the UVIT *F*154*W* and *GALEX* FUV absolute magnitudes. The following method prescribed by

Downloaded from https://academic.oup.com/mnras/article/504/3/4143/6226636 by University of Chicago user on 31 May 2021

Table 6. Estimated SFRs (in M yr^{-1}) and sSFRs (in log yr^{-1}) for the sample galaxies using various indicators. (Column 2) SFR is based on a monochromatic *IRAS* 60 μm flux converted to SFR using the conversion relation prescribed by Rowan-Robinson et al. (2008). (Column 3) SFR computed using FIR luminosity following the method given by Kewley et al. (2002). (Column 4) SFR estimated from the GMRT 610 MHz flux using the relation given by Garn et al. (2009). (Column 5) SFR computed from the UVIT *F154W* and *GALEX* FUV absolute magnitudes using the method given by Karachentsev & Kaisina (2013). (Column 6) SFR computed from the SED modelling as described in Section 5.3. (Column 7) SFR estimated using the hybrid estimator FUV and 25 μm fluxes, following the relations given by Hao et al. (2011). (Columns 8–11) SFRs and specific SFRs using the *WISE W3* and *W4* bands were obtained from the *WISE* Extended Source Catalogue by Jarrett et al. (2019).

Galaxy	60 μm[a]	FIR[a]	610 MHz[a]	FUV[a]	SED	FUV+ 25 μm	*W3*	*W4*	sSFR$_{W3}$	sSFR$_{W4}$
IC 5325	0.69 ± 0.05	0.93 ± 0.05	0.67 ± 0.05	0.44 ± 0.01	2.06 ± 0.10	1.00 ± 0.05	1.55 ± 0.60	1.14 ± 0.46	−9.93	−10.06
NGC 7496[b]	1.95 ± 0.18	1.90 ± 0.11	–	0.25 ± 0.01	1.19 ± 0.06	3.13 ± 0.24	2.25 ± 0.88	3.76 ± 1.51	−9.58	−9.36
NGC 7590[b]	1.32 ± 0.13	1.61 ± 0.10	1.27 ± 0.07	0.47 ± 0.02	2.16 ± 0.11	1.66 ± 0.11	2.15 ± 0.74	1.68 ± 0.66	−9.75	−9.86
NGC 7599	1.23 ± 0.14	1.54 ± 0.10	1.07 ± 0.07	0.55 ± 0.03	3.39 ± 0.40	1.70 ± 0.13	2.28 ± 0.88	1.65 ± 0.67	−9.68	−9.82

[a] SFR uncertainties estimated using flux uncertainties alone.
[b] Seyfert type 2 galaxies.

Karachentsev & Kaisina (2013) was used to compute the SFRs:

$$\log(\mathrm{SFR}[\mathrm{M}\ \mathrm{yr}^{-1}]) = 2.78 - 0.4 m^{c}_{\mathrm{FUV}} + 2\log(D). \qquad (6)$$

Here, m^{c}_{FUV} is the FUV magnitude corrected for extinction and D is the kinematic distance to the galaxy.

The SFRs computed using various methods are presented in Table 6. We find that SFR values obtained using radio emission are in the range 0.8 − 1.3 M yr^{-1}. The SFR estimates obtained from both FIR and radio indicators are strikingly similar despite the fact that each depends on a number of simplifying assumptions. While deriving the relation for estimating SFRs using the 60 μm luminosity, the conversion between L_{IR} and L_{60} has uncertainties in it and the parameter, , used to calculate the amount of young star formation could also vary from galaxy to galaxy. The SFR–610 MHz luminosity relation, on the other hand, bears uncertainties in the conversion of the 1.4 GHz luminosity to 610 MHz luminosity due to the assumption of a constant radio spectral index. The direct relation between non-thermal synchrotron emission and star formation is poorly understood. This is due to our lack of understanding regarding contributions of the intermediate processes, such as relations between supernova remnants and acceleration of electrons to relativistic energies, their propagation and energy loss mechanisms (Condon 1992).

Consequently, alternate measures of star formation such as in the IR are often used to derive SFR correlations in radio (Kewley et al. 2002). As thermal emission is not considered for computing the SFRs in the method by Garn et al. (2009), physical effects such as recent starburst activity or suppression of the radio luminosity in galaxies could also lead to inaccurate estimations of SFRs at radio wavelengths. The SFRs calculated using FUV emission yield the lowest values of SFRs ranging between 0.3 and 0.6 M yr^{-1}. We believe this due to the high susceptibility of FUV to extinction. SFR estimates using FUV emission can be inaccurate due to the internal light extinction in the galaxies, which would be larger in dusty galaxies such as those in our sample and is difficult to estimate. To account for this, we also estimate the SFRs for the galaxies using a hybrid SFR indicator which is a combination of the FUV and the 25 μm (MIR) fluxes (Hao et al. 2011). These SFRs range from 1.00 to 3.13 M yr^{-1}. However, we note that the SFR estimates for two of the galaxies which have an AGN are higher than the other indicators, especially for NGC 7496. This could be due to the contribution from the AGN which is also seen as excess in MIR regime. It challenging to isolate SF activity from the AGN activity and therefore difficult to obtain reliable SFR estimates for these galaxies. We have also listed the SFRs and specific star formation ratios (sSFR = SFR/mass) from the *WISE* Extended Source Catalogue (WXSC) by Jarrett et al. (2019) in Table 6 for comparison. Jarrett et al. (2019) followed the prescription given by Cluver et al. (2017) to estimate the SFRs for the galaxies using *WISE W3* (12 μm) and *W4* (22 μm) bands. The SFRs derived from the *WISE W3* and *W4* bands are significantly higher than the SFRs estimated from other methods. This method avoids uncertainties due to extinction but can produce inaccurate estimates in the presence of strong silicate absorption features in dusty starburst galaxies as well as powerful AGNs. The sSFRs from *WISE W3* and *W4* bands are not significantly different and range from −9.4 to −10.1 for our sample of galaxies. In general, the SFR estimates for NGC 7496 and NGC 7590, derived from various methods, should be interpreted with caution due to the presence of an AGN.

For local galaxies, the SFR ranges from 0.1 to 100 M yr^{-1} depending on the type of the galaxy (normal or starburst), including the MW having an SFR ∼ 1.9 ± 0.5 M yr^{-1} (Kennicutt 1998b; Chomiuk & Povich 2011). SFRs up to ∼ 20 M yr^{-1} have been estimated for gas-rich spiral galaxies (Kennicutt 1998a). In our sample, all the galaxies have relatively low SFRs, similar to the MW. The SFRs for the galaxies suggest that all of them are normal star-forming spirals. Jarrett et al. (2019) presented a galaxy star formation main-sequence (GMS) diagram, which represents the past-to-present star formation history (SFH) for galaxies (see fig. 16 of their paper). Based on the sSFR values, NGC 7590 and NGC 7599 can be placed at the upper end of the sequence as they are young, dusty galaxies with high stellar masses. By contrast, IC 5325 seems to have consumed most of its gas to attain its high stellar mass and it falls in the category of intermediate disc galaxies (like the MW and Andromeda) on the GMS diagram. NGC 7496 also falls in the same category as NGC 7590 and NGC 7599, but due to the presence of a strong AGN, one cannot be certain about its MIR derived SFR as well as the stellar mass (Jarrett et al. 2019), and hence its evolutionary stage.

4.4 Triggered star formation in NGC 7599?

NGC 7599 is a normal star-forming galaxy but shows some unusual features. NGC 7599 has faint radio emission at the nucleus, but has higher flux densities towards one of the spiral arms (Farnes, Green & Kantharia 2014). This could be associated with a recent star formation event and hence we refer to this region as an anomalous star-forming region. This anomalous star-forming region accounts for ∼ 10 per cent of the total flux from the galaxy at 610 MHz. The reason behind such high flux, which is much greater than the rest of the galaxy, is not entirely clear, but some clues are evident in the multiwavelength imaging. The region is also seen to be bright in the *WISE* imaging indicating the presence of a dusty region, as seen in star-forming regions (Jarrett et al. 2019). We suspect that this could

Downloaded from https://academic.oup.com/mnras/article/504/3/4143/6226636 by University of Chicago user on 31 May 2021

be due to the interaction with its neighbouring galaxy NGC 7590. This arm lies towards the H I ‘bridge’ found to link NGC 7599 with NGC 7590 (Freeland et al. 2009). Interactions between galaxies can perturb gas within the galaxy and lead to the formation of elongated structures like tails and bridges and can also trigger star formation in any of the interacting galaxies. The UVIT–FUV image appears to show that the anomalous star-forming region has a flux density which is marginally higher than the emission from the surrounding region in the galaxy. Because FUV imaging indicates the presence of young stars, it is possible that there is some interaction between the two galaxies which is actively triggering star formation – but in a localized, intense fashion – in the spiral arm of NGC 7599. Intriguingly, this feature does not stand out in the optical or IR images of the NGC 7599. Further investigation at higher resolution and sensitivity is required in order to better understand the origin of the anomalous star-forming region in this otherwise normal galaxy.

5 SED MODELLING

The information about various physical processes that take place in the galaxy is embedded in the SED of the galaxy. Various components (stellar, dust, nebular, etc.) contributing to the galaxy luminosity can be extracted. Therefore, a detailed analysis of the SED of a galaxy, with the aid of models, can be used to derive the various physical parameters of the galaxy (Devriendt, Guiderdoni & Sadat 1999; Popescu et al. 2011; Wild et al. 2014). In particular, SED modelling is a useful tool to understand the past and current SFH of the galaxy. In addition, SEDs furnish information about the dust luminosities, masses, emissivities, etc. and enable us to perform a detailed study of dust emission from the galaxy (Kelly et al. 2012; Lianou et al. 2019). The AGN activity in the galaxy can also be deduced from the SEDs. The SED modelling, thus, provides comprehensive information about the physical processes driving the evolution of the galaxy.

5.1 Multiwavelength data

For the SED modelling described in this section, we made use of all available photometry from UV to radio wavelengths. The multitude of photometry (Table A1) is necessary to separate the multiple blended and overlapping contributors to the SEDs, and ultimately characterize the galaxies’ cold dust content. In addition to the UVIT, GMRT, and SPT continuum measurements described in Section 3, a considerable quantity of additional photometry was assembled for our modelling effort. This includes global photometry from the *GALEX* FUV + NUV bands (Martin et al. 2005), Johnson BRI, 2MASS *JHK*$_s$ (Skrutskie et al. 2006), *WISE* bands from 3 to 22 μm (Wright et al. 2010), *IRAC* bands from 3.6 to 8.0 μm (Fazio et al. 2004), *IRAS* bands from 12 to 100 μm (Neugebauer et al. 1984), *Planck* HFI at 217, 353, 545, and 857 GHz (Planck Collaboration & Lawrence 2011), and SUMSS at 843 MHz (Mauch et al. 2003). The flux densities from FUV to NIR bands were corrected for reddening due to interstellar extinction from the MW using the method adopted by Cardelli et al. (1989). They have derived $A(\lambda)/A(V)$ for wavelengths ranging from 0.125 to 3.5 μm. Beyond this wavelength range, the extinction is relatively lower but significant. Hence, for accurate SED modelling, the extinction correction for the MIR bands (until 8.0 μm) was made using the method adopted by Indebetouw et al. (2005). The UV to NIR bands help in constraining the stellar emission, whereas the MIR to mm bands constrain the dust emission from the galaxy. The 2MASS *JHK*$_s$ and *WISE* photometry used in this work were computed in identical apertures using the custom methods described in Jarrett et al. (2003) and Jarrett et al. (2019). The radio bands are used to determine the non-thermal radio emission from the galaxy.

5.2 SED Modelling using CIGALE

The SED modelling was done using CIGALE version 0.12.1 (Ciesla et al. 2015, 2016; Boquien et al. 2019). Written in PYTHON, CIGALE can be used to model the UV to radio spectrum of galaxies easily and efficiently. It also estimates their physical properties such as SFR, stellar mass, attenuation, dust mass, dust luminosity, and AGN fraction. CIGALE provides the following categories of modules: SFH, stellar emission, nebular emission, dust attenuation, IR re-emission, AGN emission, non-thermal radio emission, and redshifting. Combining multiple modules, each component of the galaxy can be modelled explicitly and the physical parameters for the galaxy can be estimated.

The SFH of the galaxies varies from quiescent phases to episodes of intense star formation. We consider a delayed SFH where after the onset of star formation, the SFR increases nearly linearly, reaches a peak value, and then decreases smoothly. The spectrum of the composite stellar populations is calculated using the dot product of the SFH with the grid containing the evolution of the spectrum of a single stellar population (SSP). For stellar emission, we use the Bruzual & Charlot (2003) library of SSPs and the Salpeter (1955) initial mass function (IMF). The young stars emit Lyman continuum photons which ionize the surrounding gas. This energy is re-emitted in the form of a series of emission lines and a continuum, which was computed using the methods by Inoue (2011) and Inoue (2010), respectively. A major amount of the stellar emission in galaxies is attenuated by the dust grains and the energy absorbed is then re-emitted at longer wavelengths. Dust attenuation was modelled using the Calzetti et al. (2000) starburst attenuation curve, which was extended between the Lyman break and 150 nm with the Leitherer, Calzetti & Martins (2002) curve, adding a UV bump and a power law. Dust emission was modelled using the Draine et al. (2007) model and was used to calculate the dust mass.

Along with heating the dust in their birth clouds, massive young stars also produce supernova remnants which accelerate relativistic electrons in the presence of the galactic magnetic field and produce synchrotron or non-thermal radio emission. As a consequence of this, there is a nearly linear and direct relationship between star formation and cosmic ray production. This forms the basis for an FIR–radio correlation (FRC; van der Kruit 1971; Rickard & Harvey 1984; Helou, Soifer & Rowan-Robinson 1985; Condon 1992). The processes leading to the FRC are not understood in detail, and are challenging to model (Vlahakis, Eales & Dunne 2007; Lacki & Thompson 2010), but various authors have none the less developed empirical relations to define the FRC. The FRC is well established across many orders of magnitude in IR as well as radio luminosities. It is independent of redshift and holds true for various galaxy types (van der Kruit 1971; Helou et al. 1985; Yun, Reddy & Condon 2001; Seymour et al. 2009; Bourne et al. 2011; Magnelli et al. 2015; Read et al. 2018).

CIGALE employs the FRC to relate the FIR and radio emission. The non-thermal radio emission is modelled by two parameters: the radio–IR correlation coefficient $q_{\rm IR}$ (Helou et al. 1985) and the radio power-law spectral slope α. The values for the slope α were derived from the radio-frequency SEDs described in Section 4.1. For the radio–IR correlation coefficient $q_{\rm IR}$, CIGALE provides a default value of 2.58, following Helou et al. (1985), who estimated values of $q_{\rm IR}$ for a sample of spiral galaxies. As a result of an additional contribution from compact radio cores and radio jets/lobes, galaxies can have smaller $q_{\rm IR}$ values which can go as low as ∼2 (Sanders & Mirabel 1996; Yun et al. 2001). On the other hand, extreme local starbursts

Downloaded from https://academic.oup.com/mnras/article/504/3/4143/6226636 by University of Chicago user on 31 May 2021

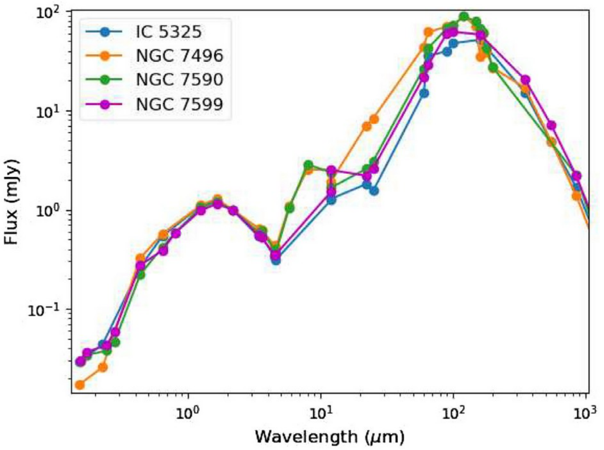

Figure 3. The multiwavelength SED for each of the galaxies in the 0.1–1000 μm range, where the fluxes for each galaxy are normalized to its 2MASS K_S band flux. The two Seyfert galaxies, NGC 7496 (orange) and NGC 7590 (green), demonstrate significantly higher fluxes in the MIR regime when compared to the two non-Seyfert galaxies, IC 5325 (blue) and NGC 7599 (magenta).

are seen to have larger dispersion in $q_{\rm IR}$ than normal star-forming galaxies (Helou et al. 1985; Condon et al. 1991; Yun et al. 2001). Condon et al. (1991) observed high $q_{\rm IR}$ for extreme starbursts. The values of $q_{\rm IR}$ can go as high as ∼ 3.0 for starbursts and mergers (Yun et al. 2001). To model the galaxies in our sample, $q_{\rm IR}$ was kept as a free parameter allowing for values both larger and smaller than the default value (see Table B1).

AGN feedback has a major impact on galaxy evolution. AGNs emit UV radiation that heats the dust in the torus and this thermal emission spectrum peaks usually in the MIR band. Ciesla et al. (2015) demonstrated that for the case of weak AGNs, the AGN–galaxy decomposition using broad-band photometry may lead to an overestimation of the AGN fraction and hence, the AGN luminosity. To avoid this, we looked at the multiwavelength photometry for both NGC 7496 and NGC 7590 in order to establish the need for an AGN component in the SED modelling process. For NGC 7496, we also see strong emission from the core at 1300 MHz, which supports the use of an AGN component to the model the SED of this galaxy.

Fig. 3 shows the multiwavelength photometry for each galaxy, normalized to the 2MASS K_S band flux for that galaxy. We see that the normalized optical–NIR fluxes are similar for all the galaxies but a strong distinction is apparent in the MIR regime. The two Seyfert galaxies, NGC 7496 and NGC 7590, show higher MIR fluxes than the other two non-AGN galaxies. This calls for the inclusion of an AGN module in the SED modelling of both NGC 7496 and NGC 7590. We use the Fritz, Franceschini & Hatziminaoglou (2006) AGN model which parametrizes the dust emission from the torus heated by the AGN.

The absorption by the intergalactic medium is computed and redshifting of the SED model is performed after computation of all the individual modules. CIGALE searches over a grid of discrete free parameter values. The free parameters used during SED modelling are given in Table B1.

5.3 Best-fitting SEDs

The best-fitting SEDs for each of our four galaxies are shown in Fig. 4, and the best-fitting parameter values are listed in Table 7. CIGALE also computes dust parameters (mass and luminosity) that are presented in Table 8. These dust masses and luminosities have been computed for the best-fitting SED models. Because CIGALE does not provide uncertainties for these quantities, we give the CIGALE Bayesian errors as indicative of the uncertainties in the best-fitting parameters. The SFRs for the galaxies have been computed by CIGALE using Bayesian statistics and are listed in Table 6. Buat et al. (2019) recently showed that, in order to reliably constrain galaxies' physical parameters, it is essential for SED models to closely approximate emission in the UV bands. Although the Buat et al. (2019) sample was at relatively high redshift, their conclusions apply generally, and are certainly germane to the analysis described here. Fortunately, for all four galaxies in our sample, the *GALEX* and *AstroSat* UV bands' emission is well modelled by our CIGALE models (Fig. 4), so we can have confidence in its treatment of the energy balance and in its derivation of the basic properties for these objects. The FIR/radio correlation coefficient for each galaxy is greater than 2.5, consistent with a lack of observed radio lobes or jets for all of them.

Below, we describe the salient features of the fits for the sources individually.

IC 5325: The SFH for IC 5325 is best fit with the oldest stellar population to be around 4000 Myr in age and with the onset of the most recent star formation activity starting around 1000 Myr ago. Stellar emission was modelled using a stellar population having a metallicity of 0.02 and a separation age of 15 Myr between the young and old stellar populations. The dust attenuation is modelled without a UV bump and exhibits a colour excess of stellar continuum light [$E(B-V)*$] for the young and old population as 0.30 and 0.05, respectively. The dust emission was modelled by using a power-law slope of 2.3, a moderate PAH fraction of 3.90, a minimum radiation field value, $U_{\rm min} = 1.5$ and 90 per cent of dust is exposed to the radiation between $U_{\rm min}$ and $U_{\rm max}$. The slope of the synchrotron emission is ∼ 0.5, and the FIR/radio correlation coefficient, $q_{\rm IR} = 2.70$. The dust mass is estimated to be 3.75×10^7 M.

NGC 7496: NGC 7496 is best modelled with an older stellar population of 5000 Myr age with the most recent burst of star formation taking place around 1000 Myr ago. The stellar population is modelled with solar metallicity and a separation of 15 Myr between the young and old stellar population. The dust attenuation is modelled without a UV bump and exhibits a colour excess of stellar continuum light [$E(B-V)*$] for young and old population as 0.45 and 0.05, respectively. The slope delta of the power law modifying the attenuation curve is 0.15. The dust emission is best modelled by using a power-law slope of 3.0, a very high PAH fraction of 6.63 and a minimum radiation field value, $U_{\rm min} = 1.5$, with 80 per cent of dust being exposed to the radiation between $U_{\rm min}$ and $U_{\rm max}$. The synchrotron emission was modelled with an FIR/radio correlation coefficient $q_{\rm IR} = 2.64$, and slope of the power law, $\alpha = 0.42$. Emission from the dusty torus of the AGN is modelled with a decreasing dust density distribution ($\propto 1/r$) along the radial direction. The galaxy exhibits a high AGN fraction (0.6) which implies higher luminosity illuminating the dusty torus. The dust mass for NGC 7496 is estimated to be 2.70×10^7 M, indicating that it is a dusty galaxy. Some excess emission is seen in the sub-mm/mm region, which hints the presence of VCD. Thus, the calculated dust mass is a lower limit to the total galaxy's dust mass.

NGC 7590: The SFH for NGC 7590 is best modelled with an old stellar population of 4000 Myr age and with the most recent star formation activity starting 1000 Myr ago. The stellar population is modelled having the solar metallicity with the difference in the ages of young and old stellar populations to be 5 Myr. The attenuation curve is modelled without a UV bump and with a colour excess

Downloaded from https://academic.oup.com/mnras/article/504/3/4143/6226636 by University of Chicago user on 31 May 2021

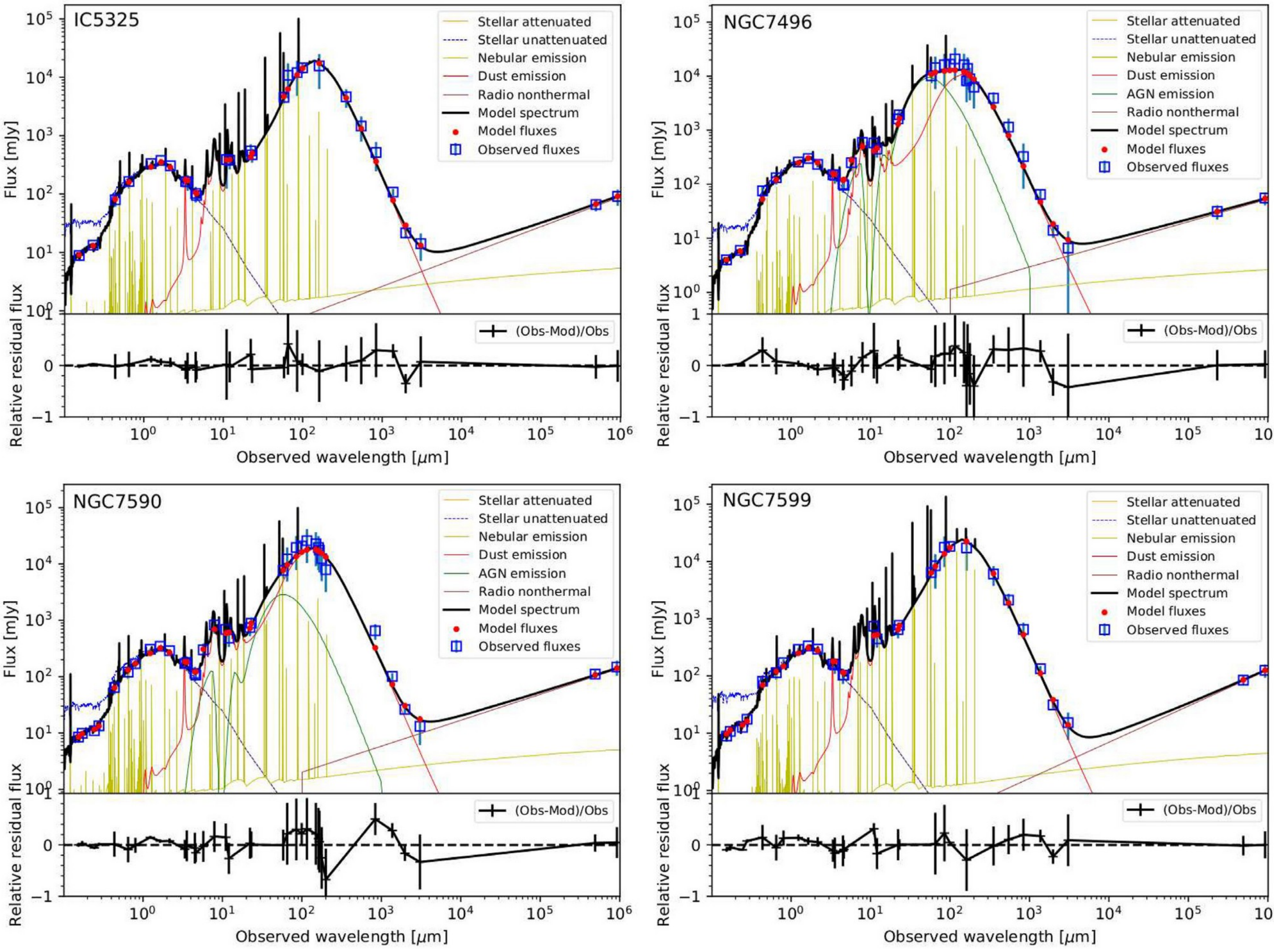

Figure 4. Best-fitting CIGALE SEDs for the four galaxies in our pilot sample. The photometry is indicated with blue boxes; the models are indicated with coloured lines. The models include unattenuated stellar emission (blue line), the AGN contribution (for NGC 7495 and NGC 7590; green line), the non-thermal radio emission, modelled with a single power-law component (maroon line), and the nebular emission (yellow-green line). The dust absorbs stellar continuum light and re-emits at longer wavelengths, as indicated by the red line. All model components are combined to construct a best-fitting model galaxy spectrum for each galaxy, indicated in black; red dots indicate the modelled fluxes in the photometric bands. Error bars are 3 σ.

of stellar light [$E(B - V)_*$] for young and old population as 0.25 and 0.10, respectively. The dust emission is modelled as a power law having a slope of 2.7, a high PAH fraction of 5.95, a minimum radiation field value $U_{\rm min}$ = 1.5, and with 60 per cent of dust being exposed to radiation between $U_{\rm min}$ and $U_{\rm max}$. The slope of the power-law non-thermal radio emission is taken to be −0.5, as obtained from the radio continuum spectra of the galaxy and the corresponding best-fitting FIR/radio correlation coefficient is $q_{\rm IR}$ = 2.51. The emission from the dusty torus of the AGN was modelled using a decreasing dust density distribution ($\propto 1/r$) along the radial direction. This galaxy exhibits a low AGN fraction (0.2) and a larger torus than NGC 7496, but has a lower dust luminosity which could be due to the insufficient heating of dust. The dust mass for the galaxy is estimated to be 3.57 × 10^7 M. From the SED, it is clearly evident that the *Planck* HFI data point are not well fit. This is a piece of evidence for the presence of a VCD component. Hence, the calculated dust mass is a lower limit to the total galaxy's dust mass.

NGC 7599: The SED for NGC 7599 is best modelled having an SFH with the oldest stars being 3500 Myr in age and the last star formation activity starting 1500 Myr ago. The stellar population was best modelled with the young and old stellar population having a metallicity of 0.05 and an age separation of 15 Myr. Using the Calzetti et al. (2000) dust attenuation law without a UV bump, the best fitting corresponds to colour excess [$E(B - V)_*$] values of 0.35 and 0.04 for young and old stellar populations, respectively. The dust emission was modelled using a power-law slope of 2.3, a moderate PAH fraction of 3.90, a minimum radiation field value $U_{\rm min}$ = 1.0, and 80 per cent of dust is exposed to the radiation between $U_{\rm min}$ and $U_{\rm max}$. For the synchrotron emission, the best fit corresponds to a slope of ~0.6 and the FIR/radio correlation coefficient, $q_{\rm IR}$ = 2.75. The dust mass for the galaxy estimated from the best fit is 7.17 × 10^7 M, which suggests that the galaxy is a very dusty galaxy and has the highest dust content in our sample of galaxies.

6 VERY COLD DUST

As is evident from Fig. 4, NGC 7496 and NGC 7590 show evidence of excess emission in the sub-mm/mm regime, relative to the best-fitting CIGALE SED models. This argues for the presence of VCD in the galaxies. Such a sub-mm excess is also seen in various low-metallicity galaxies (Chini et al. 1995; Krugel et al. 1998; Galliano et al. 2003, 2005; Marleau et al. 2006). Disney (1996) first suggested that dust grains having higher IR and FIR emissivities can achieve

Downloaded from https://academic.oup.com/mnras/article/504/3/4143/6226636 by University of Chicago user on 31 May 2021

Table 7. Best-fitting CIGALE model parameters for our sample galaxies.

Model parameters	IC 5325	NGC 7496	NGC 7590	NGC 7599
SFH				
e-folding time (Myr) of the main stellar population model	1000	1000	1000	1500
Age (Myr) of the oldest stars in the galaxy	4000	5000	4000	3500
Stellar emission				
Initial mass function	Salpeter	Salpeter	Salpeter	Salpeter
Metallicity	0.02	0.02	0.02	0.05
Age (Myr) of the separation between the young and the old star populations	15	15	5	15
Dust attenuation				
$E(B-V)*$, colour excess of stellar continuum light for young population	0.30	0.45	0.25	0.35
Reduction factor for the $E(B-V)*$ of old population as compared to young one	0.15	0.10	0.40	0.10
Amplitude of the UV bump	0.0	0.0	0.0	0.0
Slope delta of the power law modifying the attenuation curve	0.00	0.15	0.00	0.00
Dust emission				
Mass fraction of PAH (per cent)	3.90	6.63	5.95	3.90
Minimum radiation field, $U_{\rm min}$ (Habing)	1.5	1.5	1.5	1.0
Power-law slope $dU/dM \propto U^{\alpha}$, α	2.3	3.0	2.7	2.3
Fraction illuminated from $U_{\rm min}$ to $U_{\rm max}$, γ	0.1	0.2	0.4	0.2
Non-thermal radio emission				
FIR/radio correlation coefficient	2.70	2.64	2.51	2.75
Slope of non-thermal emission	0.51	0.42	0.46	0.63
Fritz et al. (2006): AGN emission				
Ratio of the maximum to minimum radii of the dust torus	–	100	100	–
Optical depth at 9.7 μm	–	10	10	–
β, power-law density distribution for radial component of torus	–	−1.0	−1.0	–
γ, power-law density distribution for polar component of torus	–	0.0	0.0	–
Full opening angle of the dust torus (deg)	–	140	100	–
Angle between equatorial axis and line of sight, ψ (deg)	–	30.1	30.1	–
AGN fraction	–	0.6	0.2	–

Table 8. Calculated parameters for dust from the best-fitting CIGALE SEDs.

Galaxy	Dust mass 10^7 M	Dust luminosity 10^{10} L	AGN torus luminosity 10^{10} L
IC 5325	3.75 ± 0.26	1.09 ± 0.05	–
NGC 7496	2.70 ± 0.30	0.79 ± 0.04	1.20 ± 0.06
NGC 7590	3.57 ± 0.38	1.32 ± 0.07	0.35 ± 0.02
NGC 7599	7.17 ± 0.61	1.74 ± 0.09	–

very low temperatures. The VCD grains are embedded deeply in the clumpy and dense molecular clouds and they are illuminated by the FIR emission from the 'classical grains' (Galliano et al. 2003; Dumke, Krause & Wielebinski 2004). Another possible explanation for these dust grains could be due to the dust grains having some unusual optical properties such as fractal or porous grains having high sub-mm/mm emissivity (Reach et al. 1995; Dumke et al. 2004). But these explanations for the very low temperature of dust grains are inconsistent with the fact that observations show VCD is distributed over galactic scales.

To estimate the VCD content in the galaxies in our sample, we added an additional very cold thermal dust component independent to the CIGALE models. The luminosity of the VCD component is calculated using the relation given by Galametz et al. (2011)

$$L_\nu^{\rm CD}(\lambda) = M_{\rm CD} 3\pi \frac{1}{\rho} \frac{Q_0}{a} \lambda_0^{\beta}[\lambda^{-\beta} B_\nu(\lambda, T_{\rm CD})], \qquad (7)$$

where $M_{\rm CD}$ is the mass of the VCD, B_ν is the *Planck* function, $T_{\rm CD}$ is the VCD temperature, $\beta = 2$ is the emissivity coefficient, $\lambda_0 = 100\,\mu$m is the reference wavelength, $\rho = 2.5 \times 10^3$ kg m^{-3} is the mass density of the grains, and $Q_0/a = 150$ cm^{-1} at λ_0 is the absorption coefficient with a as the radius of the grain. We first updated a few parameters in CIGALE to generate the CIGALE SEDs, which were then read using a PYTHON code, and a VCD component added to constrain sub-mm/mm observations and get the new SEDs that are shown in Fig. 5. Based on our initial SED modelling, the global photometry for our mm-selected galaxies is consistent with total dust masses as given in Table 8. However, SEDs do not rule out additional VCD components, the masses of which are likewise given in Table 9 for the models that include VCD components. Based on the goodness-of-fit statistics, the cold dust components did not improve the fits significantly for IC 5325 and NGC 7599. However, for NGC 7496 and NGC 7590, the additional VCD component does improve the best-fitting SEDs marginally, but the VCD does not dominate the total dust mass.

Without the constraining sub-mm/mm observations, the total dust mass could be underestimated by an order of magnitude (Galliano et al. 2005; Gordon et al. 2010). As dust grains significantly affect the molecular formation rate, cooling of the ISM as well as the SFRs in a galaxy (Hollenbach & McKee 1979; Asano et al. 2013), an inaccurate estimate of dust mass in a galaxy would lead to an erroneous interpretation of the evolution of galaxies. Devereux & Young (1990) suggested that irrespective of the ISM's phase, most of the dust grains in spiral galaxies have a temperature <15 K. These VCD grains comprise 40–70 per cent of the total dust mass

Downloaded from https://academic.oup.com/mnras/article/504/3/4143/6226636 by University of Chicago user on 31 May 2021

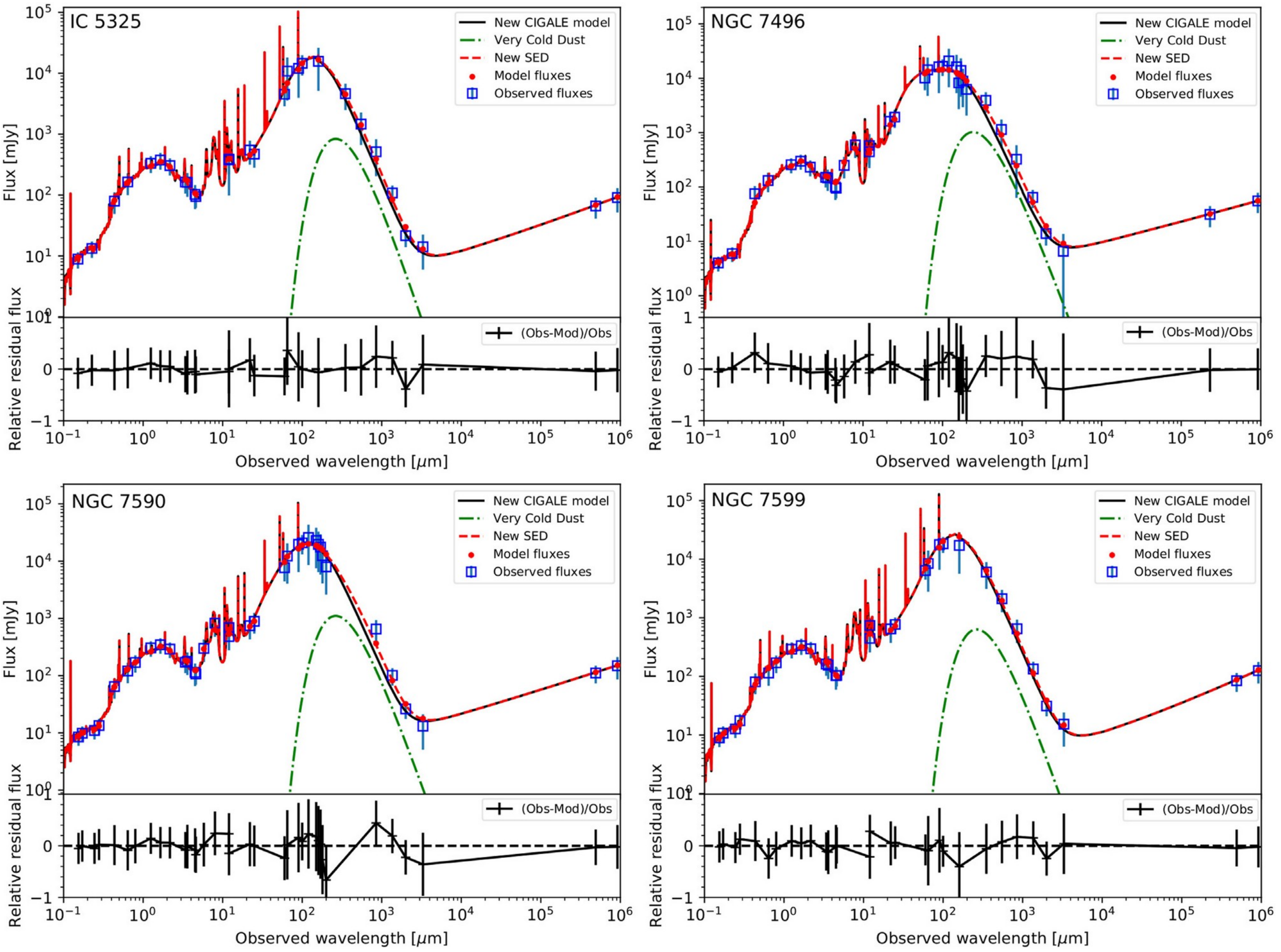

Figure 5. The new SEDs for each of the galaxies obtained (dashed red line) after adding the modifiedCIGALE model (solid black line) and the VCD component (dot–dashed green line).

Table 9. Best-fitting VCD temperatures and masses from the refined modelling.

Galaxy	Dust mass (10^7 M)	$T_{\rm VCD}{}^{a}$ (K)	VCD mass (10^7 M)	Without VCD χ^2/d.o.f.	With VCD χ^2/d.o.f.	χ 2
IC 5325	2.84 ± 0.17	$11^{+2.05}_{-3.22}$	$1.20^{+0.32}_{-0.56}$	28.35/17	27.54/15	0.81
NGC 7496	1.63 ± 0.08	$12^{+0.99}_{-1.16}$	$1.20^{+0.29}_{-0.30}$	61.20/18	55.42/16	5.78
NGC 7590	2.15 ± 0.11	$11^{+0.79}_{-1.90}$	$1.78^{+0.67}_{-0.36}$	55.65/19	49.35/17	6.30
NGC 7599	5.67 ± 0.28	$11^{+1.88}_{-2.74}$	$1.14^{+0.58}_{-0.58}$	34.20/20	33.90/18	0.30

[a] $T_{\rm VCD}$ is the temperature of the VCD component.

in the galaxy. In our sample of four galaxies, the VCD comprises no more than 15–45 per cent of the total dust mass in the galaxies. Two galaxies, IC 5325 and NGC 7599, do not have significant VCD masses. On the other hand, VCD accounts for nearly half, 40–45 per cent of the total dust content in NGC 7496 and NGC 7590, respectively. This is consistent with the values derived by Devereux & Young (1990) for a similar sample of low-redshift spiral galaxies.

7 SUMMARY

We examined some southern star-forming galaxies (IC 5325, NGC 7496, NGC 7590, and NGC 7599) in bands ranging from UV to radio. Using the GMRT observations, the radio fluxes were calculated for all the galaxies and the radio imaging of the galaxies was performed. The radio flux densities were also used to calculate the SFRs for each of the galaxies, which indicated that all the galaxies in the sample are moderate star-forming galaxies just like the MW. The radio fluxes from GMRT as well as other radio telescopes were used to estimate the radio spectral indices for the galaxies. The UVIT imaging of two of the galaxies (NGC 7590 and NGC 7599) in the sample was used to identify the young population in these galaxies. In NGC 7599, we also report the presence of an anomalous star-forming region that could be a signature of triggered star formation due to the interaction with the neighbouring galaxy, NGC 7590 (Section 4.4). SED fitting using CIGALE was used to estimate dust masses for each galaxy. We found that all four galaxies in the sample

Downloaded from https://academic.oup.com/mnras/article/504/3/4143/6226636 by University of Chicago user on 31 May 2021

have significant warmer dust components (Table 8). To estimate the sample galaxies' VCD content, we introduced a simple additional VCD component into our modelling framework and quantified the maximum VCD masses that these galaxies could contain (Table 9). VCD mass does not dominate the dust mass budgets of galaxies in our sample. Among the four, NGC 7496 and NGC 7590 show significant improvement in the SED fits when a VCD component is included. The dust masses are highly sensitive to the SED fits in the radio regime. This study, thus, highlights the importance of radio data for precise estimation of star-forming galaxies' dust content. We encourage more such studies, spanning large wavelength ranges with bigger galaxy samples for accurate estimation of cold dust content in star-forming galaxies so that its relationship to star formation activity can be better understood.

ACKNOWLEDGEMENTS

We thank the staff of GMRT, National Centre for Radio Astrophysics (NCRA) – Tata Institute of Fundamental Research (TIFR), who made the radio observations possible. This publication also uses data from the *AstroSat* mission of the Indian Space Research Organisation (ISRO), archived at the Indian Space Science Data Centre (ISSDC). This work also uses data from the SPT survey. SPT is supported by the National Science Foundation through grants PLR-1248097 and OPP-1852617. Partial support is also provided by the NSF Physics Frontier Center grant PHY-1125897 to the Kavli Institute of Cosmological Physics at the University of Chicago, the Kavli Foundation, and the Gordon and Betty Moore Foundation grant GBMF 947.

This work is based in part on observations made with the *Spitzer Space Telescope*, which is operated by the Jet Propulsion Laboratory, California Institute of Technology under a contract with NASA. This publication makes use of data products from the *Wide-field Infrared Survey Explorer*, which is a joint project of the University of California, Los Angeles, and the Jet Propulsion Laboratory/California Institute of Technology, funded by NASA. This research uses data products of the Two Micron All Sky Survey, which is a joint project of the University of Massachusetts and the Infrared Processing and Analysis Center/California Institute of Technology, funded by NASA and the NSF. This work also uses data from *Galaxy Evolution Explorer* (*GALEX*) and SUMSS surveys. *GALEX* is a NASA Small Explorer, launched in 2003 April. We gratefully acknowledge NASA's support for construction, operation, and science analysis for the *GALEX* mission, developed in cooperation with the Centre National d'Etudes Spatiales of France and the Korean Ministry of Science and Technology. We thank the Molonglo Observatory staff who are responsible for the smooth operation of the Molonglo Observatory Synthesis Telescope (MOST) and the day-to-day observing program of SUMSS. This work uses observations obtained with *Planck* (http://www.esa.int/Planck), an ESA science mission with instruments and contributions directly funded by ESA Member States, NASA, and Canada. This research has used data products from *AKARI*, a JAXA project with the participation of ESA. This research has also made use of the NED which is operated by the Jet Propulsion Laboratory, California Institute of Technology, under contract with NASA.

The authors gratefully thank the Referee and the Editors for their constructive comments and suggestions that helped improve the quality of this paper. We thank Antony Stark for his valuable comments on the manuscript. SS thanks GH, SAG; DD, PDMSA; and Director, URSC for encouragement and continuous support to carry out this research.

DATA AVAILABILITY

The data underlying this article are available in the article and the references therein.

REFERENCES

Agrawal P. C., 2004, Prog. Theor. Phys. Suppl., 155, 305
Asano R. S., Takeuchi T. T., Hirashita H., Inoue A. K., 2013, Earth Planets Space, 65, 213
Bendo G. J. et al., 2012, MNRAS, 419, 1833
Boquien M., Burgarella D., Roehlly Y., Buat V., Ciesla L., Corre D., Inoue A. K., Salas H., 2019, A&A, 622, A103
Bot C., Ysard N., Paradis D., Bernard J. P., Lagache G., Israel F. P., Wall W. F., 2010, A&A, 523, A20
Bourne N., Dunne L., Ivison R. J., Maddox S. J., Dickinson M., Frayer D. T., 2011, MNRAS, 410, 1155
Bruzual G., Charlot S., 2003, MNRAS, 344, 1000
Buat V. et al., 2010, MNRAS, 409, L1
Buat V., Ciesla L., Boquien M., Małek K., Burgarella D., 2019, A&A, 632, A79
Calzetti D., Armus L., Bohlin R. C., Kinney A. L., Koornneef J., Storchi-Bergmann T., 2000, ApJ, 533, 682
Cardelli J. A., Clayton G. C., Mathis J. S., 1989, ApJ, 345, 245
Carlstrom J. E. et al., 2011, PASP, 123, 568
Casey C. M., Narayanan D., Cooray A., 2014, Phys. Rep., 541, 45
Chini R., Kruegel E., Lemke R., Ward-Thompson D., 1995, A&A, 295, 317
Chomiuk L., Povich M. S., 2011, AJ, 142, 197
Ciesla L. et al., 2014, A&A, 565, A128
Ciesla L. et al., 2015, A&A, 576, A10
Ciesla L. et al., 2016, A&A, 585, A43
Clemens M. S. et al., 2013, MNRAS, 433, 695
Cluver M. E., Jarrett T. H., Dale D. A., Smith J. D. T., August T., Brown M. J. I., 2017, ApJ, 850, 68
Condon J. J., 1992, ARA&A, 30, 575
Condon J. J., Huang Z. P., Yin Q. F., Thuan T. X., 1991, ApJ, 378, 65
Cox P., Kruegel E., Mezger P. G., 1986, A&A, 155, 380
Dale D. A. et al., 2012, ApJ, 745, 95
Devereux N. A., Young J. S., 1990, ApJ, 359, 42
Devriendt J. E. G., Guiderdoni B., Sadat R., 1999, A&A, 350, 381
Disney M., 1996, in Block D. L., Greenberg J. M., eds, Astrophysics and Space Science Library, Vol. 209, New Extragalactic Perspectives in the New South Africa. Springer, Berlin, p. 21
Draine B. T., Lazarian A., 1998, ApJ, 508, 157
Draine B. T. et al., 2007, ApJ, 663, 866
Dumke M., Krause M., Wielebinski R., 2004, A&A, 414, 475
Everett W. B. et al., 2020, ApJ, 900, 55
Farnes J. S., Green D. A., Kantharia N. G., 2014, MNRAS, 437, 3236
Fazio G. G. et al., 2004, ApJS, 154, 10
Freeland E., Stilp A., Wilcots E., 2009, AJ, 138, 295
Fritz J., Franceschini A., Hatziminaoglou E., 2006, MNRAS, 366, 767
Galametz M. et al., 2010, A&A, 518, L55
Galametz M., Madden S. C., Galliano F., Hony S., Bendo G. J., Sauvage M., 2011, A&A, 532, A56
Galametz M. et al., 2014, MNRAS, 439, 2542
Galliano F., Madden S. C., Jones A. P., Wilson C. D., Bernard J. P., Le Peintre F., 2003, A&A, 407, 159
Galliano F., Madden S. C., Jones A. P., Wilson C. D., Bernard J. P., 2005, A&A, 434, 867
Garcia A. M., 1993, A&AS, 100, 47
Garn T., Green D. A., Riley J. M., Alexander P., 2009, MNRAS, 397, 1101
Gil de Paz A. et al., 2007, ApJS, 173, 185
Gordon K. D. et al., 2010, A&A, 518, L89
Gould R. J., Salpeter E. E., 1963, ApJ, 138, 393
Hao C.-N., Kennicutt R. C., Johnson B. D., Calzetti D., Dale D. A., Moustakas J., 2011, ApJ, 741, 124
Helou G., Soifer B. T., Rowan-Robinson M., 1985, ApJ, 298, L7

Downloaded from https://academic.oup.com/mnras/article/504/3/4143/6226636 by University of Chicago user on 31 May 2021

Hippelein A., Haas M., Lemke D., Stickel M., Tuffs R., Klaas U., Völk H., 2000, in Berkhuijsen E. M., Beck R., Walterbos R. A. M., eds, The Interstellar Medium in M31 and M33. Proceedings 232. WE-Heraeus Seminar. Shaker, Aachen, Bad Honnef, Germany, p. 81

Hollenbach D., McKee C. F., 1979, ApJS, 41, 555

Indebetouw R. et al., 2005, ApJ, 619, 931

Inoue A. K., 2010, MNRAS, 401, 1325

Inoue A. K., 2011, MNRAS, 415, 2920

Israel F. P., 1997, A&A, 328, 471

Izotov Y. I., Guseva N. G., Fricke K. J., Krügel E., Henkel C., 2014, A&A, 570, A97

Jarrett T. H., Chester T., Cutri R., Schneider S. E., Huchra J. P., 2003, AJ, 125, 525

Jarrett T. H., Cluver M. E., Brown M. J. I., Dale D. A., Tsai C. W., Masci F., 2019, ApJS, 245, 25

Juvela M., Mattila K., Lemke D., Klaas U., Leinert C., Kiss C., 2009, A&A, 500, 763

Karachentsev I. D., Kaisina E. I., 2013, AJ, 146, 46

Kelly B. C., Shetty R., Stutz A. M., Kauffmann J., Goodman A. A., Launhardt R., 2012, ApJ, 752, 55

Kennicutt R. C. J., 1983, ApJ, 272, 54

Kennicutt Robert C. J., 1998a, ARA&A, 36, 189

Kennicutt Robert C. J., 1998b, ApJ, 498, 541

Kennicutt R. C., Evans N. J., 2012, ARA&A, 50, 531

Kewley L. J., Geller M. J., Jansen R. A., Dopita M. A., 2002, AJ, 124, 3135

Kirkpatrick A. et al., 2013, ApJ, 778, 51

Koribalski B., 1996, in Skillman E. D., ed., ASP Conf. Ser. Vol. 106, The Minnesota Lectures on Extragalactic Neutral Hydrogen. Astron. Soc. Pac., San Francisco, p. 238

Krugel E., Siebenmorgen R., Zota V., Chini R., 1998, A&A, 331, L9

Lacki B. C., Thompson T. A., 2010, ApJ, 717, 196

Lagache G., Puget J.-L., Dole H., 2005, ARA&A, 43, 727

Lal D. V., Rao A. P., 2007, MNRAS, 374, 1085

Lanz L. et al., 2013, ApJ, 768, 90

Lauberts A., Valentijn E. A., 1989, The Surface Photometry Catalogue of the ESO-Uppsala Galaxies. European Southern Observatory, Garching

Laureijs R. J., Klaas U., Richards P. J., Schulz B., Abraham P., 2003, ESA SP-1262: The *ISO* Handbook, Volume IV, PHT – The Imaging Photo-Polarimeter. ESA, Noordwijk

Leitherer C., Calzetti D., Martins L. P., 2002, ApJ, 574, 114

Li A., Greenberg J. M., 2003, in Pirronello V., Krelowski J., Manicò G., eds, Proc. of the NATO ASI, Solid State Astrochemistry, Vol. 120, Kluwer, Dordrecht, p. 37

Lianou S., Barmby P., Mosenkov A., Lehnert M., Karczewski O., 2019, A&A, 631, A38

Lira P., Videla L., Wu Y., Alonso-Herrero A., Alexander D. M., Ward M., 2013, ApJ, 764, 159

Magnelli B. et al., 2015, A&A, 573, A45

Marleau F. R., Noriega-Crespo A., Rieke G., MIPS Team, 2004, American Astronomical Society Meeting 205, Vol. 36, p.1580

Marleau F. R. et al., 2006, ApJ, 646, 929

Martin D. C. et al., 2005, ApJ, 619, L1

Mathewson D. S., Ford V. L., 1996, ApJS, 107, 97

Matthews H. E., McCutcheon W. H., Kirk H., White G. J., Cohen M., 2008, AJ, 136, 2083

Mauch T., Murphy T., Buttery H. J., Curran J., Hunstead R. W., Piestrzynski B., Robertson J. G., Sadler E. M., 2003, MNRAS, 342, 1117

Misselt K. A., Gordon K. D., Clayton G. C., Wolff M. J., 2001, ApJ, 551, 277

Mocanu L. M. et al., 2013, ApJ, 779, 61

Muñoz-Mateos J. C., Gil de Paz A., Boissier S., Zamorano J., Jarrett T., Gallego J., Madore B. F., 2007, ApJ, 658, 1006

Murakami H. et al., 2007, PASJ, 59, S369

Murphy E. J. et al., 2010, ApJ, 709, L108

Netzer H., 2015, ARA&A, 53, 365

Neugebauer G. et al., 1984, ApJ, 278, L1

Pagani L., Lefèvre C., Juvela M., Pelkonen V.-M., Schuller F., 2015, A&A, 574, L5

Pilbratt G. L. et al., 2010, A&A, 518, L1

Planck Collaboration I, 2014, A&A, 571, A1

Planck Collaboration, Lawrence C. R., 2011, in American Astronomical Society Meeting Abstracts #217, 243.01

Popescu C. C., Tuffs R. J., Dopita M. A., Fischera J., Kylafis N. D., Madore B. F., 2011, A&A, 527, A109

Reach W. T. et al., 1995, ApJ, 451, 188

Read S. C. et al., 2018, MNRAS, 480, 5625

Rickard L. J., Harvey P. M., 1984, AJ, 89, 1520

Rowan-Robinson M. et al., 2008, in Chary R.-R., Teplitz H. I., Sheth K., eds, ASP Conf. Ser. Vol. 381, Infrared Diagnostics of Galaxy Evolution. Astron. Soc. Pac., San Francisco, p. 216

Rowan-Robinson M. et al., 2010, MNRAS, 409, 2

Rowlands K., Gomez H. L., Dunne L., Aragón-Salamanca A., Dye S., Maddox S., da Cunha E., van der Werf P., 2014, MNRAS, 441, 1040

Sadler E. M., Hunstead R. W., 2001, in Clowes R., Adamson A., Bromage G., eds, ASP Conf. Ser. Vol. 232, The New Era of Wide Field Astronomy. Astron. Soc. Pac., San Francisco, p. 53

Salpeter E. E., 1955, ApJ, 121, 161

Sánchez-Monge Á., Kurtz S., Palau A., Estalella R., Shepherd D., Lizano S., Franco J., Garay G., 2013, ApJ, 766, 114

Sanders D. B., Mirabel I. F., 1996, ARA&A, 34, 749

Schmitt H. R., Calzetti D., Armus L., Giavalisco M., Heckman T. M., Kennicutt R. C. J., Leitherer C., Meurer G. R., 2006, ApJ, 643, 173

Scoville N. et al., 2014, ApJ, 783, 84

Seymour N., Huynh M., Dwelly T., Symeonidis M., Hopkins A., McHardy I. M., Page M. J., Rieke G., 2009, MNRAS, 398, 1573

Singh K. P. et al., 2014, in Takahashi T., den Herder J.-W. A., Bautz M., eds, Proc. SPIE Conf. Ser. Vol. 9144, Space Telescopes and Instrumentation 2014: Ultraviolet to Gamma Ray. SPIE, Bellingham, p. 91441S

Skrutskie M. F. et al., 2006, AJ, 131, 1163

Spinoglio L., Andreani P., Malkan M. A., 2002, ApJ, 572, 105

Stark A. A., Davidson J. A., Platt S., Harper D. A., Pernic R., Loewenstein R., Engargiola G., Casey S., 1989, ApJ, 337, 650

Story K. T. et al., 2013, ApJ, 779, 86

Subramaniam A. et al., 2016, ApJ, 833, L27

Swarup G., Ananthakrishnan S., Kapahi V. K., Rao A. P., Subrahmanya C. R., Kulkarni V. K., 1991, Curr. Sci., 60, 95

Tabatabaei F. S., Weiß A., Combes F., Henkel C., Menten K. M., Beck R., Kovács A., Güsten R., 2013, A&A, 555, A128

Tandon S. N. et al., 2017a, A&A, 38, 28

Tandon S. N. et al., 2017b, AJ, 154, 128

Thilker D. A. et al., 2007, ApJS, 173, 538

Thuma G., Neininger N., Klein U., Wielebinski R., 2000, A&A, 358, 65

van der Kruit P. C., 1971, A&A, 15, 110

van Dishoeck E. F., 2004, ARA&A, 42, 119

Vieira J. D. et al., 2010, ApJ, 719, 763

Vlahakis C., Eales S., Dunne L., 2007, MNRAS, 379, 1042

Werner M. et al., 2004, American Astronomical Society Meeting Abstracts #204, 699

Whitford A. E., 1958, AJ, 63, 201

Wild V. et al., 2014, MNRAS, 440, 1880

Witt A. N., Gordon K. D., 2000, ApJ, 528, 799

Wolfire M. G., Hollenbach D., McKee C. F., Tielens A. G. G. M., Bakes E. L. O., 1995, ApJ, 443, 152

Wright E. L. et al., 2010, AJ, 140, 1868

Yamamura I. et al., 2009, in Onaka T., White G. J., Nakagawa T., Yamamura I., eds, ASP Conf. Ser. Vol. 418, AKARI, a Light to Illuminate the Misty Universe. Astron. Soc. Pac., San Francisco, p. 3

Yun M. S., Reddy N. A., Condon J. J., 2001, ApJ, 554, 803

Downloaded from https://academic.oup.com/mnras/article/504/3/4143/6226636 by University of Chicago user on 31 May 2021

APPENDIX A MULTIWAVELENGTH DATA FOR SED MODELLING

Table A1. Flux densities[a] and uncertainties (in mJy) in each band.

Bands	IC 5325	NGC 7496	NGC 7590	NGC 7599	Reference
GALEX					Gil de Paz et al. (2007)
FUV (1516 Å)	8.86 ± 0.07	4.00 ± 0.02	–	–	
NUV (2269 Å)	13.29 ± 0.11	5.97 ± 0.02	–	–	
UVIT					This work (Section 3.3)
F154W (1541 Å)	–	–	8.49 ± 0.42	8.92 ± 0.45	
F172M (1717 Å)	–	–	9.87 ± 0.49	10.78 ± 0.54	
N245M (2447 Å)	–	–	10.99 ± 0.55	12.70 ± 0.64	
N279N (2792 Å)	–	–	13.44 ± 0.67	17.53 ± 0.88	
Bessel 90					
B (4363 Å)	79.81 ± 6.44	75.25 ± 6.29	64.28 ± 5.24	80.90 ± 6.59	Lauberts & Valentijn (1989)
RC (6407 Å)	163.90 ± 13.60	131.75 ± 11.10	120.38 ± 9.99	114.12 ± 9.52	Lauberts & Valentijn (1989)
IC (7982 Å)	–	–	169.41 ± 8.23	170.50 ± 8.31	Mathewson & Ford (1996)
2MASS					Jarrett et al. (2003)
J (1.25 μm)	332.00 ± 7.02	257.00 ± 5.23	305.00 ± 2.79	291.00 ± 6.15	
H (1.65 μm)	375.00 ± 8.33	299.00 ± 6.94	345.00 ± 3.79	335.00 ± 8.05	
K_s (2.17 μm)	304.00 ± 9.29	232.00 ± 9.34	290.00 ± 4.56	295.00 ± 9.03	
WISE					Jarrett et al. (2019)
3.4 μm	163.27 ± 9.90	150.15 ± 9.10	170.75 ± 10.40	162.30 ± 11.60	
4.6 μm	94.47 ± 5.70	95.52 ± 5.80	106.68 ± 6.50	103.86 ± 6.30	
12 μm	378.30 ± 38.00	445.20 ± 44.80	481.80 ± 48.50	445.90 ± 44.80	
22 μm	547.90 ± 55.20	1617.70 ± 162.70	743.40 ± 74.80	648.10 ± 65.30	
IRAC					Fazio et al. (2004)
3.6 μm	161.56 ± 16.16	146.27 ± 14.63	177.60 ± 17.76	155.50 ± 15.55	
4.5 μm	102.23 ± 10.22	100.14 ± 10.01	114.28 ± 11.43	103.29 ± 10.33	
5.8 μm	–	250.28 ± 25.03	298.74 ± 29.87	–	
8.0 μm	–	592.80 ± 59.28	826.70 ± 82.67	–	
IRAS					NED
12 μm	390.0 ± 89.0	580.0 ± 104.3	690.0 ± 61.5	740.0 ± 78.8	
25 μm	470.0 ± 42.3	1930.0 ± 139.3	890.0 ± 75.8	770.0 ± 81.3	
60 μm	4530.0 ± 317.1	10100.0 ± 909.8	7690.0 ± 770.1	6390.0 ± 704.5	
100 μm	14 500.0 ± 1015.0	16 600.0 ± 832.7	20 800.0 ± 1459.3	18 300.0 ± 1284.0	
AKARI					Yamamura et al. (2009)
N60 (65 μm)	10 819.90 ± 2163.98	14 325.40 ± 2865.08	12 243.00 ± 2448.60	8429.10 ± 1685.82	
Wide-S (90 μm)	12 011.90 ± 2402.38	16 214.80 ± 3242.96	19 567.10 ± 3913.42	17 661.70 ± 3232.30	
N160 (160 μm)	15 642.90 ± 3128.58	8220.80 ± 1644.20	19 540.60 ± 3908.12	17 196.90 ± 3439.38	
ISOPHOT[b]					Spinoglio, Andreani & Malkan (2002)
120 μm	–	20 800 ± 4160	25 900 ± 5180	–	
150 μm	–	16 200 ± 3240	22 800 ± 4560	–	
170 μm	–	13 900 ± 2780	17 600 ± 3520	–	
180 μm	–	8890 ± 1778	12 400 ± 2480	–	
200 μm	–	6250 ± 1250	7910 ± 1582	–	
***Planck* HFI**					Planck Collaboration I (2014)
857 GHz (350 μm)	4610.8 ± 537.7	3917.8 ± 362.6	–	6031.9 ± 761.3	
545 GHz (550 μm)	1459.6 ± 222.7	1139.0 ± 167.8	–	2115.1 ± 200.2	
353 GHz (850 m)	513.9 ± 89.8	323.8 ± 80.6	651.3 ± 67.4	651.3 ± 67.4	
SPT					This work (Section 3.2)
220 GHz (1.4 mm)	108.02 ± 4.84	64.61 ± 4.62	100.95 ± 4.85	134.049 ± 5.40	
150 GHz (2.0 mm)	21.58 ± 1.35	13.98 ± 1.25	26.22 ± 1.30	31.26 ± 1.45	
95 GHz (3.2 mm)	14.16 ± 2.33	6.59 ± 2.29	13.10 ± 2.33	15.33 ± 2.57	
GMRT					This work (Section 3.1)
1300 MHz (23 cm)	–	21.40 ± 3.10	–	–	
610 MHz (49 cm)	66.00 ± 5.08	–	112.00 ± 6.14	84.50 ± 5.34	
325 MHz (92 cm)	91.00 ± 9.35	58.70 ± 5.02	148.20 ± 14.18	125.80 ± 11.00	

[a] Corrected for extinction using Cardelli et al. (1989) and Indebetouw et al. (2005) extinction laws.
[b] 20 per cent uncertainties (Laureijs et al. 2003; Juvela et al. 2009).

Downloaded from https://academic.oup.com/mnras/article/504/3/4143/6226636 by University of Chicago user on 31 May 2021

APPENDIX B FREE PARAMETERS USED DURING SED MODELLING

Table B1. Free parameters used during SED Modelling.

Model	Free parameters	Values
Delayed SF history	(1) e-folding time (Myr) of main stellar population	50, 500, 1000, 1500, 2000, 2500
	(2) Age (Myr) of the oldest stars in the galaxy	500, 1000, 1500, 2000, 2500, 3000, 3500, 4000, 4500, 5000
Stellar emission	(1) Metallicity	0.02, 0.05
	(2) Age (Myr) of the separation between the young and the old star populations	5, 10, 15
Dust attenuation	(1) $E(B-V)$, the colour excess of the stellar continuum light for the young population	0.10, 0.15, 0.20, 0.25, 0.30, 0.35, 0.40, 0.45, 0.50, 0.55, 0.60, 0.70
	(2) Reduction factor for the $E(B-V)*$ of the old population compared to the young one	0.10, 0.15, 0.20, 0.25, 0.30, 0.35, 0.40, 0.45, 0.50, 0.60, 0.70
	(3) Slope delta of the power law modifying the attenuation curve	0.00, 0.15, 0.25, 0.40, 0.50
Dust emission	(1) Mass fraction of PAH (per cent)	2.50, 3.19, 3.90, 4.58, 5.26, 5.95, 6.63, 7.32
	(2) Minimum radiation field, $U_{\rm min}$ (Habing)	0.1, 0.3, 0.5, 0.7, 0.8, 1.0, 1.5, 1.7, 2.0, 2.5, 3.0, 3.5, 4.0, 5.0, 8.0, 10.0
	(3) Power-law slope $\mathrm{d}U/\mathrm{d}M \propto U^{\alpha}, \alpha$	1.5, 1.8, 2.0, 2.3, 2.5, 2.7, 3.0
	(4) Fraction illuminated from $U_{\rm min}$ to $U_{\rm max}, \gamma$	0.1, 0.2, 0.3, 0.4, 0.5, 0.6, 0.7, 0.8
Non-thermal radio emission	(1) FIR/radio correlation coefficient	2.50–2.75
AGN torus emission	(1) Ratio of the maximum to minimum radii of the dust torus	30.0, 60.0, 100.0
	(2) Optical depth at 9.7 μm	0.1, 1.0, 3.0, 10.0
	(3) Fraction of AGN contribution to IR	0.0, 0.1, 0.2, 0.3, 0.4, 0.5, 0.6, 0.7
	(4) Full opening angle of the dust torus (deg)	60, 100, 140
	(5) β, from power-law density distribution for the radial component of the dust torus	−0.5, −1.0, 0.0
	(6) γ, from power-law density distribution for the polar component of the dust torus	0.0, 2.0

This paper has been typeset from a TEX/LATEX file prepared by the author.

Downloaded from https://academic.oup.com/mnras/article/504/3/4143/6226636 by University of Chicago user on 31 May 2021